Journal of Computational Physics 229 (2010) 5498–5517

Contents lists available at ScienceDirect

Journal of Computational Physics

journal homepage: www.elsevier.com/locate/jcp

Coupling of Dirichlet-to-Neumann boundary condition and finite difference methods in curvilinear coordinates for multiple scattering

Sebastian Acosta, Vianey Villamizar *

Department of Mathematics, Brigham Young University, Provo, UT 84602, United States

ARTICLE INFO

Article history:
Received 29 September 2009
Received in revised form 5 April 2010
Accepted 6 April 2010
Available online 11 April 2010

Keywords:
Multiple scattering
Helmholtz equation
Non-reflecting boundary condition
Curvilinear coordinates
Finite difference method
Heterogeneous media

ABSTRACT

The applicability of the Dirichlet-to-Neumann technique coupled with finite difference methods is enhanced by extending it to multiple scattering from obstacles of arbitrary shape. The original boundary value problem (BVP) for the multiple scattering problem is reformulated as an interface BVP. A heterogenous medium with variable physical properties in the vicinity of the obstacles is considered. A rigorous proof of the equivalence between these two problems for smooth interfaces in two and three dimensions for any finite number of obstacles is given. The problem is written in terms of generalized curvilinear coordinates inside the computational region. Then, novel elliptic grids conforming to complex geometrical configurations of several two-dimensional obstacles are constructed and approximations of the scattered field supported by them are obtained. The numerical method developed is validated by comparing the approximate and exact far-field patterns for the scattering from two circular obstacles. In this case, for a second order finite difference scheme, a second order convergence of the numerical solution to the exact solution is easily verified.

1. Introduction

Analytical solutions for wave scattering problems from multiple complexly shaped obstacles are not possible to obtain in general. For this reason, early work was mainly performed on circular cylindrical and spherical obstacles using modal expansions of the scattered field. The construction of analytical techniques for multiple scattering continues to be an active field of research. Numerous works on multiple scattering from circular, elliptical cylinders, and spheres have recently appeared [1–3]. A major drawback of these methods is that they cannot be applied to more general scatterer geometries. The excellent book by Martin [4] reviews a variety of these analytical techniques and contains a large number of references.

Multiple scattering from scatterers of complex geometries requires the application of numerical techniques. Recent numerical work has been based on either finite difference, integral equation, or finite element methods. For instance, Sherer and Visbal [5] and Sherer and Scott [6] discussed multiple acoustic scattering from two and three circular cylinder configurations in two dimensions. For the approximations, they employed high-order compact finite difference methods on complex grids generated by overset-meshing procedures. Their numerical solution accurately approximates the analytical solution. Although, their technique has potential applications to scatterers of arbitrary shape, they only presented results for obstacles in the form of circular cylinders. Another attempt was made by Villamizar and Acosta [7] where an acoustic scattering problem from three complexly shaped obstacles was numerically solved. The approximation obtained for the acoustic pressure field is illustrated in Fig. 1 for a two-dimensional scatterer configuration. For this purpose, the authors used

* Corresponding author. Tel.: +1 801 422 1754; fax: +1 801 378 3703.
E-mail addresses: sebastian@math.byu.edu (S. Acosta), vianey@math.byu.edu (V. Villamizar).

0021-9991/$ - see front matter © 2010 Elsevier Inc. All rights reserved.
doi:10.1016/j.jcp.2010.04.011

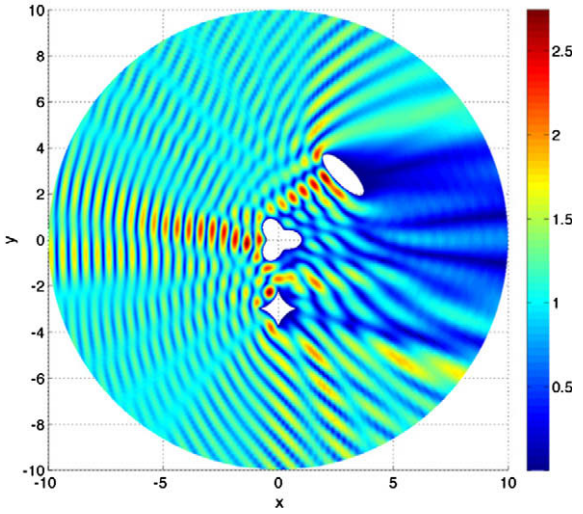

Fig. 1. Multiple acoustic scattering from three complexly shaped obstacles.

a finite difference time-dependent scheme for the wave equation in generalized curvilinear coordinates coupled with a curvilinear version of Bayliss–Gunzburger–Turkel local absorbing boundary condition [8]. Absorbing boundary conditions for scattering problems have been largely used. The potential advantages and drawbacks of these conditions have been extensively studied by Givoli [9,10], Tsynkov [11], and Medvinsky et al. [12]. In [7] as well as in [5,6], a common practice consisting of choosing an artificial boundary $\mathcal{B}$ large enough to enclose all the obstacles, where the absorbing boundary condition is placed, was followed. This practice leads to the use of relatively large domains of integration that may require huge amount of storage and computer time. Furthermore, generating appropriate grids for complex scatterer configurations may become a complicated and time consuming task as described in [7,13].

A major step to simplify the computation on regions containing complex scatterer configurations was recently taken by Grote and Kirsch [14]. Instead of employing an artificial boundary enclosing all the scatterers, they use several smaller separate artificial boundaries $\mathcal{B}^m$, each one enclosing a different obstacle. To handle the unboundedness of the physical domain, they introduced an extended version of an exact non-reflecting boundary condition known as Dirichlet-to-Neumann (DtN) [15,16]. More specifically, they defined a DtN-type condition on the artificial boundary $\mathcal{B} = \cup\mathcal{B}^m$ which they called multiple-DtN non-reflecting boundary condition. This condition is independent of the numerical discretization employed in the computational domain and of the shapes of the individual scatterers. It only depends on the shapes of the artificial boundaries. The advantage of doing this is that the computation can be performed in relatively small regions which drastically reduces the storage, computational cost, and greatly simplifies the grid generation process. Grote and Kirsch obtained remarkable numerical results for two-dimensional multiple scattering from circular and elliptical obstacles.

Our focus in this work is to take advantage of the potential that the multiple-DtN technique has to solve multiple scattering from scatterers of arbitrary shape by coupling it with a finite difference method (FDM) for the Helmholtz equation in generalized curvilinear coordinates. Furthermore, by allowing the index of refraction to vary in the vicinity of the obstacles, we are able to extend the applicability of the proposed method to complex scattering configurations dealing not only with impenetrable obstacles but also with media inhomogeneities. This is particularly important in emerging applications such as the design of special heterogeneous layers whose purpose is to shield or cloak an obstacle from electromagnetic waves to make it invisible [17,18].

An important aspect of this work is the formulation of an interface boundary value problem (BVP) equivalent to the original multiple scattering problem. The interface $\mathcal{B}$ of the new problem is formed by separate artificial boundaries $\mathcal{B}^m$ enclosing the different obstacles. For clarity and completeness, a rigorous proof of the equivalence between these two problems is given for smooth interfaces $\mathcal{B}^m$ of arbitrary shape. This equivalence is proven for acoustically soft, hard, and impedance-type impenetrable obstacles embedded in heterogeneous media. The proof is also valid in two and three dimensions for any finite number of obstacles.

The second main aspect consists of the introduction of a novel numerical technique for the efficient computation of approximate solutions to the scattering problem for geometrically complex scatterer configurations in two dimensions. The multiple-DtN condition renders a new interior BVP defined inside a region that is internally bounded by each obstacle physical boundary and externally by each artificial boundary $\mathcal{B}^m$. In fact, the complex shapes of the annular regions that forms the domain of the interior BVP leads to a reformulation of this problem in terms of generalized curvilinear coordinates. Novel elliptic conforming grids for these complex annular regions are constructed and approximations of the scattered field supported by them are obtained.

The formulation of interface problems to replace the original exterior boundary value problem for Helmholtz and other elliptic equations is not new. This procedure can be traced back to the work of Maccamy and Marin [19] which motivated the DtN non-reflecting boundary condition [15]. Similarly, Ihlenburg [20] derived the DtN technique based on an analogous interface BVP as the one discussed in the present work. Johnson and Nedelec [21] also considered an interface BVP to numerically solve Poisson's equation by coupling a finite element method (FEM) and a boundary element method (BEM) at the interfacial boundary. Most other hybrid FEM/BEM methods are based on the same procedure. In particular, the work by Hsiao [22] and the references therein follow this procedure. The technique has also been extended to problems in elasticity [23] and electromagnetism [24].

In spite of all the above work, to the best of our knowledge, there is no complete proof of this equivalence for an exterior Helmholtz problem as formulated in this article. However, there are two references where a rigorous proof of the equivalence for closely related interface problems is provided. The first one deals with the basic formulation for the Domain Decomposition Method for the Helmholtz equation as described in the pioneering work of Despres [25]. As opposed to our work, he considered an interior Helmholtz problem. The second one is the work by Monk [26] for electromagnetic scattering using the full system of Maxwell's equations.

The proposed numerical method is validated by comparing the approximate and exact far-field patterns for a configuration of two circular cylindrical obstacles. For instance, by employing a second order finite difference scheme, a second order convergence of the numerical solution to the exact solution is easily verified. Also, the method is successfully applied to three obstacles bounded by truly complex curves. This and other experiments illustrate the efficiency of the proposed technique in terms of storage (number of grid points) and computational cost. Additionally, it is well-known that volume discretizations such as FDM and FEM as opposed to boundary elements are naturally suited for treating localized heterogeneities, non-linearities, and sources. To that end, the broad scope of the method is demonstrated by applying it to complexly shaped obstacles embedded in a medium with variable index of refraction in their vicinities, which would be a difficult problem to deal with using any other numerical method.

2. Mathematical model

Consider a monochromatic plane wave, $u_{inc}(\mathbf{x})e^{-i\omega t} = e^{i\,k\mathbf{x}\cdot\mathbf{d}}e^{-i\omega t}$, where $\mathbf{d}$ is a unit vector that points in the *direction of incidence*, and $i=\sqrt{-1}$. This incident wave is impinging upon a scattering configuration of M bounded obstacles of arbitrary shape in two or three dimensions. The scatterers are assumed to be impenetrable to the acoustic waves and well separated from each other. Let Ω be the connected infinite domain bounded internally by the union of the obstacle boundaries $\mathcal{C}=\bigcup_{m=1}^{M}\mathcal{C}^m$ for $m = 1,2,\ldots,M$. These boundaries are closed smooth curves in $\mathbb{R}^2$ or surfaces in $\mathbb{R}^3$, respectively. Since the incident wave is time-harmonic, the total field can be modeled by the Helmholtz equation in the exterior region Ω.

It is assumed that the total field u satisfies the boundary condition $Z\frac{\partial u}{\partial \nu}+(1-Z)u=0$ on $\mathcal{C}$. The vector $\boldsymbol{\nu}$ represents the unit normal to the physical boundary $\mathcal{C}$ and it points into the interior of Ω. The coefficient $Z\in\mathbb{C}$ and $\mathrm{Im}(1-Z)/Z\geqslant 0$ when $Z\neq 0$. Notice that in the particular cases when $Z = 0$ or $Z = 1$, this boundary condition models acoustically soft or hard obstacles, respectively. Otherwise, it corresponds to an impedance boundary condition.

By decomposing the total field u into an incident field u_{inc} and a scattered field u_{sc} such that $u = u_{inc} + u_{sc}$ in $\overline{\Omega}$, a boundary value problem for u_{sc} is obtained. This consists of finding $u_{sc}\in C^2(\Omega)\cap C(\overline{\Omega})$, satisfying

$$\Delta u_{sc}+k^2n^2(\mathbf{x})u_{sc}=k^2m(\mathbf{x})u_{inc}\quad \text{in } \Omega, \tag{1}$$

$$Z\frac{\partial u_{sc}}{\partial \nu}+(1-Z)u_{sc}=-\left(Z\frac{\partial u_{inc}}{\partial \nu}+(1-Z)u_{inc}\right)\quad \text{on } \mathcal{C}, \tag{2}$$

$$\lim_{r\to\infty} r^{(\delta-1)/2}\left(\frac{\partial u_{sc}}{\partial r}-iku_{sc}\right)=0, \tag{3}$$

where $k > 0$ is the *wavenumber*, $n\in C^1(\Omega)\cap C(\overline{\Omega})$ is a real-valued function called the *index of refraction*, and $m := 1-n^2$ has compact support K. The limit in (3), known as the Sommerfeld radiation condition, is assumed to hold uniformly for all directions, where $r = |\mathbf{x}|$ and the parameter $\delta = 2$ or 3 for two or three dimensions, respectively.

In this work, two important physical cases modeled by the above BVP will be considered. One of them is for a homogeneous ($n\equiv 1$) exterior region Ω surrounding the obstacles, while the other one is for a heterogeneous exterior region where n is allowed to vary only in the immediate vicinity of the obstacles, and $n(\mathbf{x}) = 1$ in the rest of the domain. It is possible to show existence and uniqueness for (1)–(3) using some of the theorems in [27]. In fact, the field, $u_{sc} = u_1 + u_2$, uniquely solves BVP (1)–(3) provided that u_1 is the radiating solution to the Helmholtz equation in Ω satisfying the boundary condition (2), and u_2 is the radiating field satisfying

$$\Delta u_2+k^2u_2=k^2m(\mathbf{x})u_2+k^2m(\mathbf{x})(u_1+u_{inc})\quad \text{in } \Omega, \tag{4}$$

as well as the homogeneous boundary condition corresponding to (2). The existence and uniqueness of such u_1 is proven in Chapter 3 of [27]. Regarding u_2, consider the Lippmann–Schwinger integral equation

$$u_2(\mathbf{x})+k^2\int_K G(\mathbf{x},\mathbf{y})m(\mathbf{y})u_2(\mathbf{y})d\mathbf{y}=-k^2\int_K G(\mathbf{x},\mathbf{y})m(\mathbf{y})(u_1(\mathbf{y})+u_{inc}(\mathbf{y}))d\mathbf{y}, \tag{5}$$

where $G(\mathbf{x},\mathbf{y})$ is the radiating Green's function satisfying Helmholtz equation ($n \equiv 1$) in Ω when $\mathbf{x} \neq \mathbf{y}$, as well as the homogeneous boundary condition corresponding to (2). This Green's function G can be constructed according to Chapter 9 in [28]. For the existence and uniqueness of u_2, it is enough to show first, that the BVP for u_2 is equivalent to the problem of solving the integral Eq. (5) and secondly, that this integral equation has a unique solution. The proof of the equivalence follows closely the one for Theorem 8.3 in [27], with the fundamental solution replaced by the Green's function. Similarly, existence and uniqueness of solutions for (5), readily follows from Section 8.3 in [27].

An important aspect of this work is the formulation of an interface BVP equivalent to (1)–(3). A second aspect deals with the introduction of a novel numerical technique for the efficient computation of the solution of this interface BVP for geometrically complex configurations. The next section is dedicated to the formulation of the equivalent BVP.

3. An equivalent interface boundary value problem

In this section, an equivalence between the original boundary value problem (1)–(3) and an associated interface boundary value problem is rigorously established. The formulation of the interface BVP will be performed in two dimensions where $\mathbf{x} = (x,y) \in \mathbb{R}^2$, with corresponding polar coordinates (r,θ) such that $x = r\cos\theta$ and $y = r\sin\theta$. However, this formulation can be easily extended to three dimensions.

3.1. Interface boundary value problem

First, a domain decomposition is stated in preparation for the formulation of the equivalent interface problem. The domain Ω is divided into the following sub-domains:

(i) Several bounded open disjoint sub-domains Ω^m ($m = 1,2,\ldots,M$), which are internally bounded by a closed curve $\mathcal{C}^m$ and externally bounded by another closed curve, denoted by $\mathcal{B}^m$, as shown in Fig. 2. From these sub-domains a bounded physical domain Ω_{in} is defined as $\Omega_{in} = \bigcup_{m=1}^{M} \Omega^m$. Also, by joining all the outer curves, an interface $\mathcal{B} = \bigcup_{m=1}^{M} \mathcal{B}^m$ is obtained. For computational convenience, the curves $\mathcal{B}^m$ are chosen as circles. However, the theory that will be developed in this Section 3.1 and the next Section 3.2 is valid for sufficiently smooth closed curves.

(ii) An open unbounded connected exterior region $\Omega_{out} = \Omega \setminus \overline{\Omega}_{in}$.

To simplify the notation, open unbounded connected exterior regions $\Psi^m = \Omega \setminus \overline{\Omega^m}$ ($m = 1,2,\ldots,M$) are also introduced. Notice that $\Omega_{out} = \bigcap_{m=1}^{M} \Psi^m$, and that points enclosed by the curves $\mathcal{C}^l$ belong to Ψ^m if $l \neq m$. Also, the interface between Ω^m and Ω_{out} is the circle denoted by $\mathcal{B}^m$ of radius R^m centered at the point $\mathcal{O}^m$. It is assumed that the obstacles are well separated, such that the circles $\mathcal{B}^m$ do not intersect each other and Ω_{out} is connected.

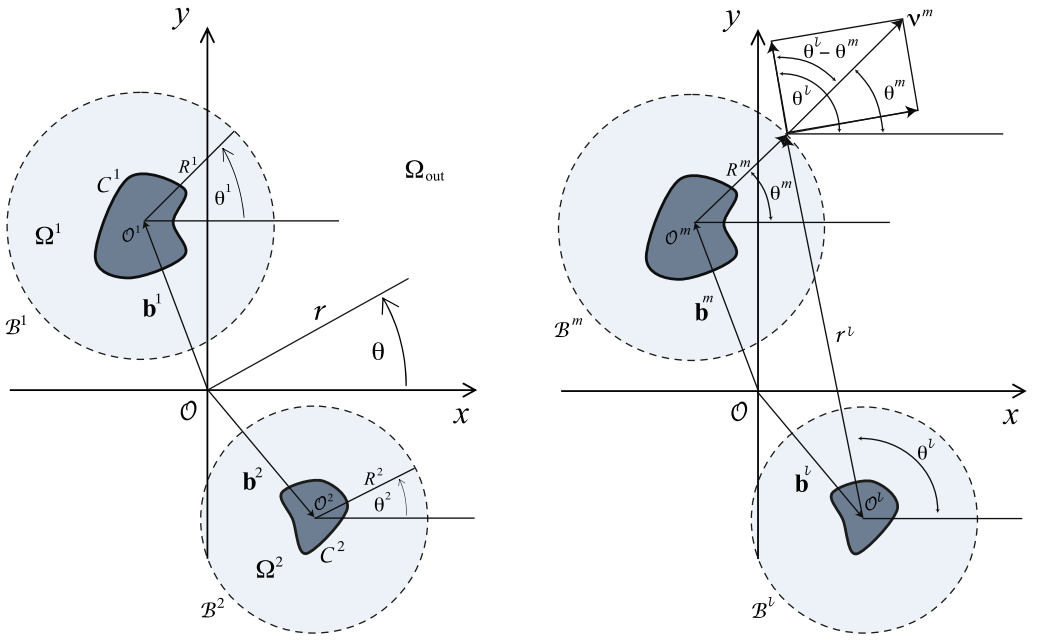

Fig. 2. Domain decomposition with interface curves, and global system of coordinates (left). Coordinates of the normal vector at a point on $\mathcal{B}^m$ with respect to l-polar coordinates (r^l,θ^l) (right).

Now, an *interface boundary value problem* is defined. This problem consists of finding $u_{in} \in C^2(\Omega_{in}) \cap C(\overline{\Omega}_{in})$ and $u_{out} \in C^2(\Omega_{out}) \cap C(\overline{\Omega}_{out})$ satisfying

$$\Delta u_{in} + k^2 n^2(\mathbf{x}) u_{in} = k^2 m(\mathbf{x}) u_{inc} \quad \text{in } \Omega_{in}, \tag{6}$$

$$\Delta u_{out} + k^2 u_{out} = 0 \quad \text{in } \Omega_{out}. \tag{7}$$

Physical boundary condition:

$$Z \frac{\partial u_{in}}{\partial \nu} + (1 - Z) u_{in} = -\left(Z \frac{\partial u_{inc}}{\partial \nu} + (1 - Z) u_{inc} \right) \quad \text{on } \mathcal{C}. \tag{8}$$

Sommerfeld radiation condition:

$$\lim_{r \to \infty} \sqrt{r} \left(\frac{\partial u_{out}}{\partial r} - iku_{out} \right) = 0, \quad \text{uniformly for all } \theta \in [0, 2\pi]. \tag{9}$$

Interface conditions:

$$u_{in} = u_{out} \quad \text{on } \mathcal{B}, \tag{10}$$

$$\frac{\partial u_{in}}{\partial \nu} = \frac{\partial u_{out}}{\partial \nu} \quad \text{on } \mathcal{B}, \tag{11}$$

with n, m, and Z as already defined in Section 2. The interface $\mathcal{B}$ is chosen so that the support of m is contained in Ω_{in}. The unit normal vector $\boldsymbol{\nu}$ points into Ω_{in} in (8) and into Ω_{out} in (11). It will be shown below that this interface BVP is equivalent to the original multiple scattering BVP (1)–(3) by proving that both problems have the same unique solution in their common domain Ω. Other similar approaches to transform the original BVP into an equivalent interface BVP that is easier to treat numerically have been used by other researchers, as mentioned in Section 1.

For clarity and completeness, a rigorous proof of the equivalence between (1), (2), (7)–(10) and (11) is presented in the rest of this section. The formulation and proof of Theorem 1, discussed below, is inspired in a similar one found in [14]. The strategy of the proof consists of showing that the solution u_{sc} of (1)–(3) is also a solution of (6)–(11) followed by a proof of uniqueness.

Theorem 1. *The interface boundary value problem (6)–(11) has a unique solution given by u_{in} in $\overline{\Omega}_{in}$ and u_{out} in $\overline{\Omega}_{out}$, such that u_{in} coincides with the restriction of the solution of (1)–(3) u_{sc} to $\overline{\Omega}_{in}$, and u_{out} coincides with the restriction of u_{sc} to $\overline{\Omega}_{out}$.*

Proof. *Existence*. As mentioned above there is a unique solution $u_{sc} \in C^2(\Omega) \cap C(\overline{\Omega})$ to the scattering problem (1)–(3). Due to the regularity of u_{sc} in Ω, the fact that Ω_{in} contains the support of m, and that Ω_{in}, Ω_{out}, and $\mathcal{B}$ are contained in Ω, it follows that u_{sc} is also a solution to the interface BVP (6)–(11).

Uniqueness. Here, it is sufficient to show that any solution to the homogeneous interface BVP associated to (6)–(11) vanishes identically. So, let two complex-valued functions $w_{in} \in C^2(\Omega_{in}) \cap C(\overline{\Omega}_{in})$ and $w_{out} \in C^2(\Omega_{out}) \cap C(\overline{\Omega}_{out})$ satisfy the homogeneous interface BVP. Applying Green's first identity to w_{in} and $\overline{w}_{in}$ in the region Ω_{in} leads to

$$\int_{\mathcal{B}} w_{in} \frac{\partial \overline{w}_{in}}{\partial \nu} dl - \int_{\mathcal{C}} w_{in} \frac{\partial \overline{w}_{in}}{\partial \nu} dl = \int_{\Omega_{in}} |\nabla w_{in}|^2 ds + \int_{\Omega_{in}} w_{in} \Delta \overline{w}_{in} ds. \tag{12}$$

Using Helmholtz equation for w_{in}, substituting the interface continuity conditions into the integral over $\mathcal{B}$, and solving for this term yields

$$\int_{\mathcal{B}} w_{out} \frac{\partial \overline{w}_{out}}{\partial \nu} dl = \int_{\Omega_{in}} |\nabla w_{in}|^2 ds - \int_{\Omega_{in}} k^2 n^2 |w_{in}|^2 ds + \int_{\mathcal{C}} w_{in} \frac{\partial \overline{w}_{in}}{\partial \nu} dl. \tag{13}$$

Considering only its imaginary part, Eq. (13) reduces to

$$\mathrm{Im}\left(\int_{\mathcal{B}} w_{out} \frac{\partial \overline{w}_{out}}{\partial \nu} dl \right) = \mathrm{Im}\left(\int_{\mathcal{C}} w_{in} \frac{\partial \overline{w}_{in}}{\partial \nu} dl \right). \tag{14}$$

On the boundary $\mathcal{C}$, w_{in} satisfies the homogenous condition $Z \frac{\partial w_{in}}{\partial \nu} + (1 - Z) w_{in} = 0$. Assuming $Z \neq 0$, solving for the derivative term and substituting it into (14) results in

$$\mathrm{Im}\left(\int_{\mathcal{B}} w_{out} \frac{\partial \overline{w}_{out}}{\partial \nu} dl \right) = \mathrm{Im}\left(\frac{1 - Z}{Z} \right) \left(\int_{\mathcal{C}} |w_{in}|^2 dl \right) \geqslant 0. \tag{15}$$

Applying Theorem 2.12 in [27] (which is a direct consequence of Rellich's lemma) to w_{out} leads to the conclusion $w_{out} = 0$ in $\overline{\Omega}_{out}$. For the special case when $Z = 0$ (Dirichlet condition), the hypothesis of Theorem 2.12 is trivially satisfied from (14). Also, the continuity conditions at the interface $\mathcal{B}$ lead to $w_{in} = w_{out} = 0$ and $\frac{\partial w_{in}}{\partial \nu} = \frac{\partial w_{out}}{\partial \nu} = 0$ on $\mathcal{B}$.

Now, it only remains to show that $w_{in} = 0$ in $\overline{\Omega}_{in}$. This is accomplished by the use of Green's integral representation of w_{in}, derived in Theorem 2.1 of [27]. In fact for $\mathbf{x} \in \Omega_{in}$,

$$w_{in}(\mathbf{x}) = \int_{\mathcal{C}} \left[w_{in}(\mathbf{y}) \frac{\partial \Phi(\mathbf{x},\mathbf{y})}{\partial \nu(\mathbf{y})} - \Phi(\mathbf{x},\mathbf{y}) \frac{\partial w_{in}}{\partial \nu}(\mathbf{y}) \right] dl(\mathbf{y}) - \int_{\Omega_{in}} k^2 m(\mathbf{y}) w_{in}(\mathbf{y}) \Phi(\mathbf{x},\mathbf{y}) ds(\mathbf{y}). \tag{16}$$

Here, Φ is the fundamental solution to Helmholtz equation. By letting $\mathbf{x}$ vary throughout $\Omega_{in} \cup \overline{\Omega}_{out} = \Omega$ in the right-hand side of (16), an extension $\tilde{w}$ of w_{in} defined in the entire unbounded region Ω can be readily constructed. Due to the regularity of the integrands of (16) in Ω_{out}, the extension $\tilde{w}|_{\Omega_{out}} \in C^2(\Omega_{out}) \cap C(\overline{\Omega}_{out})$, and it is clearly a radiating solution to the Helmholtz equation in this region. Moreover, $\tilde{w} = w_{in} = 0$ on $\mathcal{B}$. Therefore, another application of Theorem 2.12 in [27] leads to $\tilde{w} = 0$ in Ω_{out}.

Furthermore, the first integral in (16) satisfies Helmholtz equation in Ω. Also since $m \in C^1(\Omega) \cap C(\overline{\Omega})$ with its support contained in Ω_{in}, and $w_{in} \in C^2(\Omega_{in}) \cap C(\overline{\Omega}_{in})$ then, Theorem 8.1 in [27] applied to the volume potential in (16) guarantees, first, that $\tilde{w}$ is in $C^2(\Omega)$, and secondly, that $\Delta\tilde{w} + k^2 n^2(\mathbf{x})\tilde{w} = 0$ in Ω. Since $\tilde{w}$ already vanishes in Ω_{out}, all conditions of Theorem 8.6 in [27] (unique continuation principle) are satisfied which lead to the vanishing of $\tilde{w}$ in the entire domain Ω. Hence, the sought condition, $w_{in} = \tilde{w}|_{\Omega_{in}} = 0$ in $\overline{\Omega}_{in}$, is obtained completing the proof of uniqueness.

In the course of the proof of existence, it has been shown that u_{sc}, the solution to (1)–(3), is also the solution to (6)–(11). To complete the proof of the equivalence between the two problems, the reciprocal statement should be proved. For this purpose, consider a pair of functions u_{in} and u_{out} forming the solution $\tilde{u}_{sc}$ to the interface BVP (6)–(11), *i.e.*,

$$\tilde{u}_{sc}(\mathbf{x}) := \begin{cases} u_{in}(\mathbf{x}), & \text{if } \mathbf{x} \in \overline{\Omega}_{in}; \\ u_{out}(\mathbf{x}), & \text{if } \mathbf{x} \in \overline{\Omega}_{out}. \end{cases} \tag{17}$$

If $\tilde{u}_{sc}$ were not the solution to (1)–(3), then u_{sc} and $\tilde{u}_{sc}$ would be two different solutions of the interface BVP (6)–(11) contradicting the uniqueness just proven. □

Remark 1. The proof of Theorem 1 can easily be extended to three dimensions by making the appropriate changes in the interface, the integrals involved and the radiation condition. It also applies to obstacles embedded in heterogeneous media with variations of the index of refraction in their vicinity. Furthermore, by eliminating the physical boundary $\mathcal{C}$ and letting Ω_{in} be the region enclosed by $\mathcal{B}$, the proof of Theorem 1 also applies to multiple scattering by heterogeneous media in the absence of impenetrable obstacles.

Due to the complexity of the above interface BVP in terms of the boundary shape, number, and position of the obstacles, an explicit analytical solution cannot be found in general. Therefore, this problem should be treated by numerical methods, in general. One of the main difficulties encountered by numerical methods based on finite difference or finite element is the efficient handling of the unboundedness of the physical domain. The next section deals with this difficulty.

3.2. Derivation of the multiple-DtN boundary condition

The advantage of replacing the original scattering problem (1)–(3) by the interface BVP (6)–(11) is that its solution can be worked out in two different forms and regions. First, numerical solutions are sought inside the complexly bounded annular regions Ω^m and then an analytical solution is completely determined in the outer region Ω_{out} which is internally bounded by the artificial boundaries $\mathcal{B}^m$. As a result, the computational cost is greatly reduced since the computation can be performed in relatively smaller regions.

Details on how to obtain both forms of the solution are as follows. First, obtain an analytical expression for u_{out} in the unbounded sub-domain Ω_{out} depending on unknown boundary values at $\mathcal{B}$. Second, use the interface conditions (10) and (11) and the analytical expression of u_{out}, evaluated at the interface $\mathcal{B}$, to derive a non-reflecting boundary condition called the multiple-DtN condition [14] for u_{in} on $\mathcal{B}$. Then, use this boundary condition, (6) and (8) to define a new BVP in the bounded domain Ω_{in}. Third, numerically solve for u_{in} in Ω_{in} and for the boundary data of u_{out} on $\mathcal{B}$. Finally, replace the boundary values of u_{out} at $\mathcal{B}$ into the analytical expression for u_{out} to completely determine u_{out} in Ω_{out}. From the formula for u_{out}, the far-field pattern may be computed if desired.

To derive an analytical expression for u_{out} in $\overline{\Omega}_{out}$, we follow the approach in [14]. This consists of defining a family of M purely outgoing wave fields $u^m \in C^2(\Psi^m) \cap C(\overline{\Psi^m})$ $(m = 1,\ldots,M)$ satisfying

$$\Delta u^m + k^2 u^m = 0 \quad \text{in } \Psi^m, \tag{18}$$

$$\lim_{r\to\infty} \sqrt{r}\left(\frac{\partial u^m}{\partial r} - iku^m \right) = 0. \tag{19}$$

Each outgoing wave u^m is uniquely determined by its boundary data at $\mathcal{B}^m$, as shown in Chapter 3 of [27]. The next theorem states that u_{out} can be represented as a superposition of purely outgoing wave fields u^m.

Theorem 2. *Let $u_{out} \in C^2(\Omega_{out}) \cap C(\overline{\Omega}_{out})$ be part of the unique solution to the interface BVP (6)–(11) in Ω_{out}. Then, u_{out} can be uniquely decomposed into M purely outgoing wave fields $u^m (m = 1,2,\ldots,M)$, i.e.,*

$$u_{out}(\mathbf{x}) = \sum_{m=1}^{M} u^m(\mathbf{x}), \quad \mathbf{x} \in \overline{\Omega}_{out}, \tag{20}$$

satisfying (18) and (19).

Proof. *Existence*. Following Grote and Kirsch [14], let us define each purely outgoing wave field by

$$u^m(\mathbf{x}) := \int_{\mathcal{B}^m} \left[u_{out}(\mathbf{y}) \frac{\partial \Phi(\mathbf{x},\mathbf{y})}{\partial \nu(\mathbf{y})} - \Phi(\mathbf{x},\mathbf{y}) \frac{\partial u_{out}}{\partial \nu}(\mathbf{y}) \right] dl(\mathbf{y}) \quad \text{for } \mathbf{x} \in \Psi^m. \tag{21}$$

The goal is to show that the outgoing wave fields defined by (21) satisfy Eqs. (18)–(20). To begin, each $u^m \in C^2(\Psi^m)$, since $\Phi(\mathbf{x},\mathbf{y})$ as a function of $\mathbf{x}$ also belongs to $C^2(\Psi^m)$. Furthermore, defining u^m on $\mathcal{B}^m$ as the continuous extension (see the *jump relations* Theorem 3.1 of [27]) of the integral (21) leads to $u^m \in C^2(\Psi^m) \cap C(\overline{\Psi^m})$.

Now, considering Green's integral representation of u_{out} in Ω_{out} and using the additivity of the integral over the domain $\mathcal{B} = \bigcup_{m=1}^M \mathcal{B}^m$, we obtain

$$\begin{aligned} u_{out}(\mathbf{x}) &= \int_{\mathcal{B}} \left[u_{out}(\mathbf{y}) \frac{\partial \Phi(\mathbf{x},\mathbf{y})}{\partial \nu(\mathbf{y})} - \Phi(\mathbf{x},\mathbf{y}) \frac{\partial u_{out}}{\partial \nu}(\mathbf{y}) \right] dl(\mathbf{y}) = \sum_{m=1}^M \int_{\mathcal{B}^m} \left[u_{out}(\mathbf{y}) \frac{\partial \Phi(\mathbf{x},\mathbf{y})}{\partial \nu(\mathbf{y})} - \Phi(\mathbf{x},\mathbf{y}) \frac{\partial u_{out}}{\partial \nu}(\mathbf{y}) \right] dl(\mathbf{y}) \\ &= \sum_{m=1}^M u^m(\mathbf{x}), \quad \mathbf{x} \in \Omega_{out}. \end{aligned} \tag{22}$$

Thus, the decomposition of u_{out} into M outgoing waves u^m in $\overline{\Omega}_{out}$ has been proved. Next, we will show that this decomposition is unique.

Uniqueness. Assume there is another decomposition of u_{out} in terms of outgoing waves $v^m \in C^2(\Psi^m) \cap C(\overline{\Psi^m})$ ($m = 1,\ldots,M$) satisfying (18) and (19). Then,

$$\sum_{l=1}^M w^l = \sum_{l=1}^M (u^l - v^l) = u_{out} - u_{out} = 0 \quad \text{in } \overline{\Omega}_{out}. \tag{23}$$

To prove uniqueness, it is sufficient to show that for an arbitrary $m \in \{1,2,\ldots,M\}$, $w^m := u^m - v^m \equiv 0$ in $\overline{\Psi^m}$. This can be accomplished by constructing an open and connected region Υ^m bounded internally by $\mathcal{B}^m$ and externally by some simple, closed, smooth curve $\mathcal{H}^m$ that does not intersect any of the components of the interface boundary $\mathcal{B}$. This is possible because the obstacles are well separated from each other. Then, it follows that $\Upsilon^m \subset \Omega_{out}$.

The key idea of the proof is that $w^l (l \neq m)$ satisfies Helmholtz equation at every point inside the region bounded by $\mathcal{H}^m$ including points inside the obstacle enclosed by $\mathcal{C}^m$. Whereas, w^m satisfies Helmholtz equation at every point outside the region enclosed by $\mathcal{H}^m$, as well as the radiation condition at infinity. As a result, Green's integral representation of w^m on the unbounded region internally bounded by $\mathcal{H}^m$ yields

$$\int_{\mathcal{H}^m} \left[w^m(\mathbf{y}) \frac{\partial \Phi(\mathbf{x},\mathbf{y})}{\partial \nu(\mathbf{y})} - \Phi(\mathbf{x},\mathbf{y}) \frac{\partial w^m}{\partial \nu}(\mathbf{y}) \right] dl(\mathbf{y}) = 0 \quad \text{for } \mathbf{x} \in \Upsilon^m. \tag{24}$$

Also, the integral representation of w^l on the bounded region with outer boundary $\mathcal{H}^m$ leads to

$$\int_{\mathcal{H}^m} \left[w^l(\mathbf{y}) \frac{\partial \Phi(\mathbf{x},\mathbf{y})}{\partial \nu(\mathbf{y})} - \Phi(\mathbf{x},\mathbf{y}) \frac{\partial w^l}{\partial \nu}(\mathbf{y}) \right] dl(\mathbf{y}) = -w^l(\mathbf{x}) \quad \text{for } \mathbf{x} \in \Upsilon^m \quad \text{and} \quad l \neq m. \tag{25}$$

Then, adding (25) for all $l \neq m$ and (24) results

$$\int_{\mathcal{H}^m} \left[\sum_{l=1}^M w^l(\mathbf{y}) \frac{\partial \Phi(\mathbf{x},\mathbf{y})}{\partial \nu(\mathbf{y})} - \Phi(\mathbf{x},\mathbf{y}) \frac{\partial \sum_{l=1}^M w^l}{\partial \nu}(\mathbf{y}) \right] dl(\mathbf{y}) = -\sum_{l \neq m} w^l(\mathbf{x}), \quad \mathbf{x} \in \Upsilon^m. \tag{26}$$

Notice that $\mathcal{H}^m \subset \Omega_{out}$, then the result in (23) can be used at the left of (26) leading to $\sum_{l \neq m} w^l(\mathbf{x}) = 0$ for all $\mathbf{x} \in \Upsilon^m$. Finally, by comparing this sum with (23), it follows that $w^m(\mathbf{x}) = 0$ for all $\mathbf{x} \in \Upsilon^m$. Since w^m vanishes in the open region Υ^m, then it vanishes in the entirety of its domain of definition $\overline{\Psi^m}$, due to its analyticity (see Theorem 2.2 in [27]). From the arbitrariness of m, it follows that $w^m \equiv 0$ for all $m \in \{1,2,\ldots,M\}$ which establishes the uniqueness of the decomposition. □

Remark 2. The proof of Theorem 2 does not require the interfaces $\mathcal{B}^m$ to be circles. The knowledge of the eigenfunctions corresponding to a particular geometry is not needed in the course of the proof. It is almost identical in three dimensions by making the appropriate changes in the interface, the integrals involved, and the radiation condition.

The decomposition (20) of u_{out} and the interface conditions (10) and (11) on $\mathcal{B}$ lead to the definition of the multiple-DtN non-reflecting boundary condition introduced in [14]. In fact, a new interior boundary value problem for $u_{in} \in C^2(\Omega_{in}) \cap C(\overline{\Omega}_{in})$ and for the boundary values of u^m ($m = 1,2,\ldots,M$) on $\mathcal{B}^m$ is defined as

$$\nabla^2 u_{in} + k^2 n^2(\mathbf{x}) u_{in} = k^2 m(\mathbf{x}) u_{inc} \quad \text{in } \Omega_{in}, \tag{27}$$

$$Z \frac{\partial u_{in}}{\partial \nu} + (1 - Z) u_{in} = -\left(Z \frac{\partial u_{inc}}{\partial \nu} + (1 - Z) u_{inc} \right) \quad \text{on } \mathcal{C}, \tag{28}$$

$$u_{in} = \sum_{l=1}^M u^l \quad \text{on } \mathcal{B}^m \quad \text{for } m = 1,2,\ldots,M, \tag{29}$$

$$\frac{\partial u_{in}}{\partial \nu^m} = \sum_{l=1}^{M} \frac{\partial u^l}{\partial \nu^m} \quad \text{on } \mathcal{B}^m \quad \text{for } m = 1, 2, \ldots, M, \tag{30}$$

where $\boldsymbol{\nu}$, the unit normal vector to $\mathcal{C}$, points into the interior of Ω_{in} and $\boldsymbol{\nu}^m$, the unit normal vector to $\mathcal{B}^m$, points into the exterior of Ω^m. The two equations (29) and (30) constitute the multiple-DtN boundary condition.

The integral representation (21) of u^m was enough to prove Theorem 2, but it is not convenient for computational purposes. An alternative useful representation of these outgoing waves can be obtained for separable regions. For instance, if the interface boundary components $\mathcal{B}^m$ are chosen to be circles (two-dimensional case), and local polar coordinate systems (r^m, θ^m) are defined in the outer regions Ψ^m internally bounded by $\mathcal{B}^m$, then, the outgoing fields u^m can be written in terms of eigenfunction expansions and their boundary values on $\mathcal{B}^m$ as follows:

$$u^m(r^m, \theta^m) = \frac{1}{2\pi} \sum_{n=0}^{\infty} \epsilon_n \frac{H_n^{(1)}(kr^m)}{H_n^{(1)}(kR^m)} \int_0^{2\pi} u^m(R^m, \tilde{\theta}) \cos n(\theta^m - \tilde{\theta}) d\tilde{\theta}, \tag{31}$$

where $R^m \leqslant r^m$, $0 \leqslant \theta^m \leqslant 2\pi$, and ϵ_n is the Neumann factor, *i.e.*, $\epsilon_0 = 1$ and $\epsilon_n = 2$ for $n \geqslant 1$. This expression for u^m is replaced in (29) and (30) to obtain explicit representations of the multiple-DtN boundary condition. As mentioned above, the BVP (27)–(30) is numerically solved and the boundary values of u^m on $\mathcal{B}^m$ are obtained as a by-product. These values are replaced into (31) to obtain u^m in Ψ^m and ultimately u_{out} in Ω_{out} from the decomposition (20). As shown in Theorem 3 of [14], the far-field pattern u_∞ of u_{out} is given by

$$u_\infty(\theta) = \frac{1 - i}{2\pi\sqrt{\pi}} \sum_{m=1}^{M} \sum_{n=0}^{\infty} \epsilon_n \frac{(-i)^n e^{-ik(b_x^m \cos\theta + b_y^m \sin\theta)}}{H_n^{(1)}(kR^m)} \int_0^{2\pi} u^m(R^m, \tilde{\theta}) \cos n(\theta - \tilde{\theta}) d\tilde{\theta}. \tag{32}$$

For other scattering configurations, for example elongated obstacles, it might be convenient to use other curves/surfaces, such as ellipses/ellipsoids, as the interfaces $\mathcal{B}^m$ (see [16]). As long as an analytical representation of the outgoing wave fields similar to (31) is available, the interior BVP (27)–(30) can be defined and then numerically solved. Thus, the theory and techniques formulated in this work are not limited to circular (or spherical) interfaces.

Notice that the validity of the theorems presented in this section is based on the existence of a unique solution to the original scattering BVP (1)–(3). In [27], the existence of strong solutions is proven using potential theory, Fredholm integral equations of the second kind, and the Riesz–Fredholm theory for compact operators. That work requires the physical boundary $\mathcal{C}$ to be of class $\mathcal{C}^2$. If this assumption is relaxed, that approach is no longer valid in general. Unfortunately, in practical applications is common to find boundaries with corners and edges. Existence of solutions for these singular boundaries has been studied [29], but for brevity, they are not discussed in this work.

Regarding the use of finite difference methods for regions containing boundary singularities, such as re-entrant corners, it is well-known that the expected rate of convergence or even convergence may not be achieved in general. For instance, for convergent methods the gradients in the vicinity of the singularity may become unbounded thus negatively affecting the rate of convergence. In particular, this is the case for the FDM supported by curvilinear boundary-conforming coordinates introduced in this work. To alleviate this difficulty several approaches have been devised depending on the type of singularity. Good references are found in [30,31] for finite differences and also in [32,33], for finite elements. In most of these approaches, a coupling of the analytical and numerical solutions about the singularity is performed (similar to the DtN approach at the interface). The implementation of these techniques in connection with the curvilinear FDM is a work yet to be done. However, in Section 6.2, the proposed FDM coupled with the multiple-DtN technique was successfully applied to several multiple scattering configurations including singularities on their boundaries. Although we have not performed a rigorous study, we attribute the convergence of these numerical experiments to the smoothness and the boundary-conforming properties of the elliptic grids employed.

4. Multiple scattering problem in generalized curvilinear coordinates

A goal of the present work is to obtain accurate and efficient numerical solutions of multiple scattering problems from complexly shaped obstacles in two dimensions. As outlined in the previous sections, the proposed approach consists of obtaining a numerical approximation of the BVP (27)–(30) in a relatively small bounded region $\Omega_{in} = \bigcup_{m=1}^{M} \Omega^m$, see Fig. 2. Each sub-domain Ω^m is an annular region with arbitrary piecewise smooth inner boundary $\mathcal{C}^m$ and circular outer boundary $\mathcal{B}^m$. Local boundary-conforming curvilinear coordinate systems are defined for each sub-domain $\overline{\Omega^m}$. Thus, the coordinate lines conform to the corresponding obstacle bounding curve $\mathcal{C}^m$ and to the outer circle $\mathcal{B}^m$. These local systems of coordinates are independent from each other.

The coordinates of a point in the bounded sub-domain $\overline{\Omega^m}$ are given by

$$\mathbf{x}(\xi^m, \eta^m) = (x(\xi^m, \eta^m), y(\xi^m, \eta^m)), \quad \text{where } 1 \leqslant \xi^m \leqslant N_1^m \quad \text{and} \quad 1 \leqslant \eta^m \leqslant N_2^m.$$

The parametric curves $(x(\xi^m, 1), y(\xi^m, 1))$ and $(x(\xi^m, N_2^m), y(\xi^m, N_2^m))$ coincide with the boundary curves $\mathcal{C}_m$ and $\mathcal{B}_m$, respectively. The new coordinates may be obtained as transformations T^m from a computational domain with rectangular coordinates

(ξ^m,η^m) to the physical sub-domain $\overline{\Omega^m}$ with coordinates $(x(\xi^m,\eta^m),y(\xi^m,\eta^m))$. The transformations T^m are smooth and invertible. They are defined in more detail in Section 5.1.

In contrast, for each unbounded region $\overline{\Psi^m}=\Omega\setminus\Omega^m$ local polar coordinate systems

$$\mathbf{x}(r^m,\theta^m)=(x(r^m,\theta^m),y(r^m,\theta^m))=\mathbf{b}^m+(r^m\cos\theta^m,r^m\sin\theta^m),\quad m=1,2,\ldots,M \tag{33}$$

are constructed. Here, $R^m\leqslant r^m<\infty$ and $0\leqslant\theta^m\leqslant 2\pi$ are the independent variables in polar coordinates measured from the center, $\mathbf{b}^m=(b_x^m,b_y^m)$, of the circle $\mathcal{B}^m$. Thus, any point in $\overline{\Omega}_{out}=\bigcap_{m=1}^{M}\overline{\Psi^m}$ has a different representation for each $m\in\{1,2,\ldots,M\}$. As a consequence, the location of any point in Ω can be given in terms of either the independent variables (r^m,θ^m) or (ξ^m,η^m), depending on where it is located. More precisely,

$$\mathbf{x}=(x,y)=\begin{cases}\mathbf{b}^m+(r^m\cos\theta^m,r^m\sin\theta^m), & \text{if } \mathbf{x}\in\overline{\Psi^m};\\ (x(\xi^m,\eta^m),y(\xi^m,\eta^m)), & \text{if } \mathbf{x}\in\overline{\Omega^m};\end{cases}\quad m=1,2,\ldots,M. \tag{34}$$

Notice that an arbitrary point on the circular interface $\mathcal{B}^m$, may be identified using both ordered pairs (r^m,θ^m) and (ξ^m,η^m). In fact, on the circle $\mathcal{B}^m$, the variables r^m and η^m adopt the following values $r^m=R^m$, $\eta^m=N_2^m$. Thus, $\mathbf{x}(R^m,\theta^m)=\mathbf{x}(\xi^m,N_2^m)$ when $\mathbf{x}\in\mathcal{B}^m$.

The interior BVP (27)–(30) in generalized curvilinear coordinates is governed by Eq. (27) defined in the union of M disjoint sub-domains Ω^m written in terms of (ξ^m,η^m), respectively. Dropping the m superscript, each governing equation becomes

$$\begin{aligned}&\frac{1}{J^2}\Big(\alpha(u_{in})_{\xi\xi}-2\beta(u_{in})_{\xi\eta}+\gamma(u_{in})_{\eta\eta}\Big)+\frac{1}{J^3}\Big(\alpha y_{\xi\xi}-2\beta y_{\xi\eta}+\gamma y_{\eta\eta}\Big)\Big(x_\eta(u_{in})_\xi-x_\xi(u_{in})_\eta\Big)\\&\quad+\frac{1}{J^3}\Big(\alpha x_{\xi\xi}-2\beta x_{\xi\eta}+\gamma x_{\eta\eta}\Big)\Big(y_\xi(u_{in})_\eta-y_\eta(u_{in})_\xi\Big)+k^2n^2(\xi,\eta)u_{in}=k^2m(\xi,\eta)u_{inc},\end{aligned} \tag{35}$$

where $n(\xi,\eta)=n(\mathbf{x}(\xi^m,\eta^m))$ with similar notation for $m(\xi,\eta)$. The symbols α, β, γ, and J represent the scale metric factors and the jacobian of the coordinates transformation T^m, respectively. These are defined as

$$\alpha=x_\eta^2+y_\eta^2,\quad \beta=x_\xi x_\eta+y_\xi y_\eta,\quad \gamma=x_\xi^2+y_\xi^2,\quad \text{and}\quad J=x_\xi y_\eta-x_\eta y_\xi.$$

Also, the normal derivatives of u_{in} and u_{inc}, present in the boundary condition (28), can be written at each portion $\mathcal{C}^m$ of the physical boundary in terms of (ξ^m,η^m) for $\eta^m=1$ as

$$\frac{\partial u_{in}}{\partial\nu^m}(\xi^m)=(\boldsymbol{\nu}^m\cdot\nabla u_{in})(\mathbf{x}(\xi^m,1))=\frac{1}{\sqrt{\gamma}}\begin{pmatrix}-y_\xi\\ x_\xi\end{pmatrix}\cdot\frac{1}{J}\begin{pmatrix}(u_{in})_\xi y_\eta-(u_{in})_\eta y_\xi\\ (u_{in})_\eta x_\xi-(u_{in})_\xi x_\eta\end{pmatrix}\quad\text{and} \tag{36}$$

$$\frac{\partial u_{inc}}{\partial\nu^m}(\xi^m)=(\boldsymbol{\nu}^m\cdot\nabla u_{inc})(\mathbf{x}(\xi^m,1))=\frac{1}{\sqrt{\gamma}}\begin{pmatrix}-y_\xi\\ x_\xi\end{pmatrix}\cdot ik\mathbf{d}e^{ik\mathbf{x}\cdot\mathbf{d}}, \tag{37}$$

where the definition of the incident field u_{inc} has been used in (37). However, for the two-dimensional problem, it is convenient to express $\mathbf{d}=(\cos\phi,\sin\phi)$ where ϕ is called the *angle of incidence* of the incident plane wave. Substitution of (36) and (37) into boundary condition (28) at the physical boundary $\mathcal{C}^m$ leads to

$$Z\Big[\gamma(u_{in})_\eta-\beta(u_{in})_\xi\Big]+(1-Z)\sqrt{\gamma}Ju_{in}=\big[ikZ(y_\xi\cos\phi-x_\xi\sin\phi)-(1-Z)\sqrt{\gamma}\big]Je^{ik(x\cos\phi+y\sin\phi)}, \tag{38}$$

where x, y, x_ξ, y_ξ, γ, β, J, u_{in}, $(u_{in})_\xi$, and $(u_{in})_\eta$ are functions of (ξ^m,η^m) and should be evaluated at $\eta^m=1$, which corresponds to the physical boundary $\mathcal{C}^m$.

At each interface $\mathcal{B}^m$, boundary condition (29) requires the evaluation of the outgoing wave fields u^l $(l=1,\ldots,M)$ at points $\mathbf{x}(\xi^m,N_2^m)$ on the circle as follows:

$$u^l(\xi^m)=u^l(\mathbf{x}(\xi^m,N_2^m))=u^l(\mathbf{x}(r^l(\xi^m,N_2^m),\theta^l(\xi^m,N_2^m))=\frac{1}{2\pi}\sum_{n=0}^{\infty}\epsilon_n\frac{H_n^{(1)}(kr^l(\xi^m))}{H_n^{(1)}(kR^l)}\int_0^{2\pi}u^l(R^l,\tilde\theta)\cos n(\theta^l(\xi^m)-\tilde\theta)d\tilde\theta, \tag{39}$$

where $r^l(\xi^m)=r^l(\xi^m,N_2^m)$ and $\theta^l(\xi^m)=\theta^l(\xi^m,N_2^m)$ are uniquely determined from ξ^m. Notice that for $l=m$ (39) reduces to (31).

The left-hand side of boundary condition (30) requires the evaluation of the derivative of u_{in} in the direction normal to each $\mathcal{B}^m$. Since $\mathcal{B}^m$ is a circle of radius R^m centered at (b_x^m,b_y^m), it is easier to obtain the components of the unit vector $\boldsymbol{\nu}^m$ in terms of the coordinates of the global Cartesian system as $\boldsymbol{\nu}^m=(1/R^m)(x-b_x^m,y-b_y^m)$. Consequently, the derivative of u_{in} in the direction normal to $\mathcal{B}^m$ becomes

$$\frac{\partial u_{in}}{\partial\nu^m}(\xi^m)=(\boldsymbol{\nu}^m\cdot\nabla u_{in})(\mathbf{x}(\xi^m,N_2^m))=\frac{1}{R^m}\begin{pmatrix}x-b_x^m\\ y-b_y^m\end{pmatrix}\cdot\frac{1}{J}\begin{pmatrix}(u_{in})_\xi y_\eta-(u_{in})_\eta y_\xi\\ (u_{in})_\eta x_\xi-(u_{in})_\xi x_\eta\end{pmatrix}=\frac{1}{R^mJ}\Big(\mu(u_{in})_\xi+\lambda(u_{in})_\eta\Big), \tag{40}$$

where $\mu=(x-b_x^m)y_\eta-(y-b_y^m)x_\eta$ and $\lambda=(y-b_y^m)x_\xi-(x-b_x^m)y_\xi$. Here again, x, y, x_ξ, y_ξ, x_η, y_η, J, $(u_{in})_\xi$, and $(u_{in})_\eta$ are functions of the independent variables (ξ^m,η^m) and they should be evaluated at $\eta^m=N_2^m$ which corresponds to the artificial boundary $\mathcal{B}^m$.

At the right-hand side of (30), the normal derivatives of the outgoing wave fields u_l ($l = 1,\ldots,M$) in the direction normal to $\mathcal{B}^m$ are present. Their expressions in terms of generalized coordinates (ξ^m,η^m) changes depending if $l = m$ or $l \neq m$. For $l = m$, the normal derivative is in the radial direction of the local m-polar coordinates (r^m,θ^m). Therefore, they can be evaluated directly from (31) as

$$\frac{\partial u^m}{\partial \nu^m}(\xi^m) = \frac{\partial u^m}{\partial r^m}(\mathbf{x}(\xi^m, N_2^m)) = \frac{k}{2\pi}\sum_{n=0}^{\infty}\epsilon_n \frac{H_n^{(1)'}(kR^m))}{H_n^{(1)}(kR^m)}\int_0^{2\pi} u^m(R^m,\tilde{\theta})\cos n(\theta^m(\xi^m)-\tilde{\theta})d\tilde{\theta}. \tag{41}$$

When $l \neq m$, it is more convenient to write the unit vector $\boldsymbol{\nu}^m$ in terms of the l-polar coordinates (r^l,θ^l). As illustrated in Fig. 2, its components are $\boldsymbol{\nu}^m = (\cos[\theta^l(\xi^m)-\theta^m(\xi^m)],\ -\sin[\theta^l(\xi^m)-\theta^m(\xi^m)])$. This leads to the following expression for the normal derivative:

$$\begin{aligned}\frac{\partial u^l}{\partial \nu^m}(\xi^m) &= (\boldsymbol{\nu}^m\cdot\nabla u^l)(\mathbf{x}(\xi^m,N_2^m)) = \begin{pmatrix}\cos[\theta^l(\xi^m)-\theta^m(\xi^m)]\\ -\sin[\theta^l(\xi^m)-\theta^m(\xi^m)]\end{pmatrix}\cdot\begin{pmatrix}\frac{\partial u^l}{\partial r^l}\\ \frac{1}{r^l}\frac{\partial u^l}{\partial \theta^l}\end{pmatrix}\\ &= \cos[\theta^l(\xi^m)-\theta^m(\xi^m)]\frac{k}{2\pi}\sum_{n=0}^{\infty}\epsilon_n\frac{H_n^{(1)\prime}(kr^l(\xi^m))}{H_n^{(1)}(kR^l))}\int_0^{2\pi}u^l(R^l,\tilde{\theta})\cos n(\theta^l(\xi^m)-\tilde{\theta})d\tilde{\theta}\\ &\quad+\frac{\sin[\theta^l(\xi^m)-\theta^m(\xi^m)]}{2\pi r^l(\xi^m)}\sum_{n=0}^{\infty}\epsilon_n\frac{nH_n^{(1)}(kr^l(\xi^m))}{H_n^{(1)}(kR^l)}\int_0^{2\pi}u^l(R^l,\tilde{\theta})\sin n(\theta^l(\xi^m)-\tilde{\theta})d\tilde{\theta}.\end{aligned} \tag{42}$$

Since the transformation of coordinates represented by (34) is invertible, then the ordered pair (r^l,θ^l) and the angle θ^m that appear in Eqs. (39) and (42) are uniquely determined from ξ^m. In particular, $\mathbf{x}(\xi^m,N_2^m) = \mathbf{x}(R^m,\theta^m) = \mathbf{x}(r^l,\theta^l)$. A more explicit relationship between (r^l,θ^l) and ξ^m is given by

$$r^l = \sqrt{\left(x(\xi^m,N_2^m)-b_x^l\right)^2+\left(y(\xi^m,N_2^m)-b_y^l\right)^2}, \tag{43}$$

$$\cos(\theta^l) = \frac{x(\xi^m,N_2^m)-b_x^l}{r^l},\quad \sin(\theta^l) = \frac{y(\xi^m,N_2^m)-b_y^l}{r^l}, \tag{44}$$

whereas the dependence of θ^m on ξ^m is given by

$$\cos(\theta^m) = \frac{x(\xi^m,N_2^m)-b_x^m}{R^m},\quad \sin(\theta^m) = \frac{y(\xi^m,N_2^m)-b_y^m}{R^m}. \tag{45}$$

However, the dependence of x and y on ξ^m is determined numerically or analytically only after the transformation T^m is defined.

The results of this section can be summarized as a reformulation of the interior BVP (27)–(30) in terms of generalized curvilinear coordinates. The new formulation consists of (35) as governing equation with (38) as physical boundary condition, (29) as part of the multiple-DtN boundary condition, where $u^l(\xi^m)$ is given by (39) and (30) as the other equation forming the multiple-DtN condition, with the normal derivative terms replaced by (40)–(42). Each one of these equations need to be considered over each sub-domain Ω^m.

5. Numerical solution: grids and finite difference method

As mentioned in the introduction, the BVP in generalized curvilinear coordinates just derived will be numerically solved using finite difference methods. This approach requires robust supporting grids for the accuracy of the approximate solutions. Therefore, there is a need to obtain appropriate grids for scatterers of complexly shaped geometry. The approach adopted in this work consists of generating structured elliptic grids numerically. This is done through a transformation T^m used to establish a relationship between the coordinates (ξ^m,η^m) in a rectangular computational domain and the physical coordinates (x,y) in $\overline{\Omega^m}$.

5.1. Numerical grid generation: elliptic-polar grids

A precise definition for the transformation T^m is given in this section. The generation of elliptic coordinates for the sub-domain Ω^m is independent from the generation in other sub-domains Ω^l. Therefore, results in this section are applicable to all Ω^m, $m \in \{1,2,\ldots,M\}$. In order to alleviate the notation, the superscripts will be dropped at this point and reassumed later when necessary. A common practice in elliptic grid generation is to implicitly define the transformation T as the numerical solution to a Dirichlet boundary value problem governed by the following system of quasi-linear elliptic equations [34,35] for the physical coordinates x and y,

$$\alpha x_{\xi\xi} - 2\beta x_{\xi\eta} + \gamma x_{\eta\eta} + \alpha\psi x_\xi + \gamma\phi x_\eta = 0, \tag{46}$$

$$\alpha y_{\xi\xi} - 2\beta y_{\xi\eta} + \gamma y_{\eta\eta} + \alpha\psi y_\xi + \gamma\phi y_\eta = 0. \tag{47}$$

The functions ψ and ϕ are called control functions for the influence they have on the location of the grid lines of the final grid. Their appropriate definition has been the subject of numerous studies. A few of them are found in [13,36,37].

For annular regions with circular boundaries, the optimum uniform smooth grid is the one obtained using polar coordinates. This is the preferred grid in most applications when boundary layers are not present. A natural question to ask is if there is a particular way to define ψ and ϕ such that the generalized curvilinear coordinates generated from (46) and (47) for circular annular domains coincides with the well-known polar coordinates. The answer to this question is positive. Actually, by defining the control functions $\psi = \frac{\alpha_\xi(\xi,\eta)}{2\alpha(\xi,\eta)}$ and $\phi = \frac{\gamma_\eta(\xi,\eta)}{2\gamma(\xi,\eta)}$, the elliptic system (46) and (47) transforms into

$$\alpha x_{\xi\xi} - 2\beta x_{\xi\eta} + \gamma x_{\eta\eta} + \frac{1}{2}\alpha_\xi x_\xi + \frac{1}{2}\gamma_\eta x_\eta = 0, \tag{48}$$

$$\alpha y_{\xi\xi} - 2\beta y_{\xi\eta} + \gamma y_{\eta\eta} + \frac{1}{2}\alpha_\xi y_\xi + \frac{1}{2}\gamma_\eta y_\eta = 0. \tag{49}$$

As stated in the next theorem, a particular solution to this system is provided by the well-known polar coordinates. First, consider the polar coordinates defined by the transformation

$$x(\xi,\eta) = b_x + r(\eta)\cos\theta(\xi), \quad y(\xi,\eta) = b_y + r(\eta)\sin\theta(\xi), \tag{50}$$

where

$$r(\eta) = \frac{R-a}{N_2-1}(\eta-1) + a, \quad \theta(\xi) = \frac{2\pi}{N_1-1}(\xi-1), \quad 1 \leqslant \xi \leqslant N_1, \quad 1 \leqslant \eta \leqslant N_2.$$

Obviously, the plane region corresponding to transformation (50) consists of the circular annular region with center at $\mathbf{b} = (b_x, b_y)$, inner radius a, and outer radius R.

Theorem 3. *The BVP for the coordinates $(x,y) = (x(\xi,\eta), y(\xi,\eta))$ governed by the quasi-linear elliptic equations (48) and (49) with boundary conditions given by*

$$(x(\xi,1), y(\xi,1)) = \mathbf{b} + (a\cos\theta(\xi), a\sin\theta(\xi)), \tag{51}$$

$$(x(\xi,N_2), y(\xi,N_2)) = \mathbf{b} + (R\cos\theta(\xi), R\sin\theta(\xi)), \tag{52}$$

$$(x(1,\eta), y(1,\eta)) = (x(N_1,\eta), y(N_1,\eta)), \tag{53}$$

$$(x_\xi(1,\eta), y_\xi(1,\eta)) = (x_\xi(N_1,\eta), y_\xi(N_1,\eta)), \quad 1 \leqslant \xi \leqslant N_1, \quad 1 \leqslant \eta \leqslant N_2 \tag{54}$$

has polar coordinates given by transformation (50) as a solution.

Proof. First, notice that coordinates (50) satisfy the boundary conditions (51) and (52) and the conditions of periodicity (53) and (54). A straightforward differentiation shows that they also satisfy the governing elliptic partial differential Eqs. (48) and (49). Therefore, these polar coordinates are a solution to the boundary value problem governed by this elliptic system. □

A natural expectation is that grids generated from (48) and (49) for non-circular annular regions preserve the good properties that polar grids have for circular domains. In fact, this is the case, as shown for all the particular domains considered in this work. Therefore, these new elliptic grids can be considered as a generalization of the polar grids to more complex annular regions. Thus, we will call them *elliptic-polar grids*.

The numerical grid generation process consists of using centered finite difference approximation combined with point-SOR iteration. For convenience, the independent variables ξ and η are discretized using a unit step size $\Delta\xi = \Delta\eta = 1$, and their discrete values are $\xi_i = i\Delta\xi = i$ and $\eta_j = j\Delta\eta = j$ where $i = 1,2,\ldots,N_1$ and $j = 1,2,\ldots,N_2$. The grid size is denoted by $N_1 \times N_2$. A refinement of the discretization is then obtained by increasing N_1 and N_2 as desired. In particular, the physical coordinate x of any interior grid point is obtained from the numerical solution of the following discrete equation in iterative form

$$x_{ij}^{k+1} = \frac{1}{2(\alpha+\gamma)_{ij}}\left[\alpha_{ij}(x_{i+1\,j}^{k} + x_{i-1\,j}^{k+1}) + \gamma_{ij}(x_{ij+1}^{k} + x_{ij-1}^{k+1}) + \left(2x_\xi x_\eta x_{\xi\eta} + y_{\xi\eta}(x_\xi y_\eta + x_\eta y_\xi)\right)_{ij} - 2\beta_{ij}(x_{\xi\eta})_{ij}\right], \tag{55}$$

where

$$\alpha_{ij} = (x_\eta)_{ij}^2 + (y_\eta)_{ij}^2, \quad \beta_{ij} = (x_\xi)_{ij}(x_\eta)_{ij} + (y_\xi)_{ij}(y_\eta)_{ij}, \quad \gamma_{ij} = (x_\xi)_{ij}^2 + (y_\xi)_{ij}^2,$$

and

$$(x_\xi)_{ij} = (x_{i+1\,j}^{k} - x_{i-1\,j}^{k+1})/2, \quad (x_\eta)_{ij} = (x_{ij+1}^{k} - x_{ij-1}^{k+1})/2,$$
$$(y_\xi)_{ij} = (y_{i+1\,j}^{k} - y_{i-1\,j}^{k+1})/2, \quad (y_\eta)_{ij} = (y_{ij+1}^{k} - y_{ij-1}^{k+1})/2,$$
$$(x_{\xi\eta})_{ij} = (x_{i+1\,j+1}^{k} - x_{i+1\,j-1}^{k} - x_{i-1\,j+1}^{k+1} + x_{i-1\,j-1}^{k+1})/4,$$
$$(y_{\xi\eta})_{ij} = (y_{i+1\,j+1}^{k} - y_{i+1\,j-1}^{k} - y_{i-1\,j+1}^{k+1} + y_{i-1\,j-1}^{k+1})/4,$$

for $i = 2,\ldots,N_1 - 1$ and $j = 2,\ldots,N_2 - 1$.

A similar algebraic equation is obtained for the discrete values of the y-coordinate. The super-indices k and $k+1$ represent the current and new steps in the iteration process. The SOR method [38] uses a relaxation parameter ϖ to update x_{ij}^{k+1} value

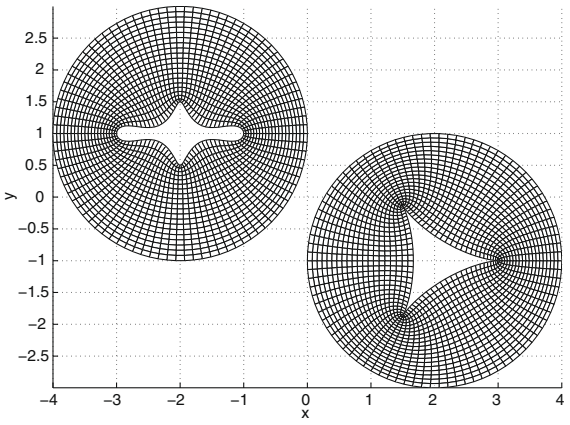

Fig. 3. Elliptic-polar grids for two complexly shaped scatterers.

as $x_{i,j}^{k+1} = \varpi x_{i,j}^{k+1} + (1-\varpi)x_{i,j}^{k}$. The value of $\varpi = 1.80$ is appropriate for relatively fast convergence of the iterative technique. At $k = 0$, an initial grid needs to be defined. Then, new grids are iteratively obtained until the maximum pointwise error between two consecutive grids falls under some specified tolerance, *i.e.*, $\epsilon^{k+1} < Tol$. This maximum pointwise error is defined as follows:

$$\epsilon^{k+1} = \max_{\substack{1\leqslant i\leqslant N_1\\ 1\leqslant j\leqslant N_2}} \left\{ |x_{i,j}^{k+1} - x_{i,j}^{k}|, |y_{i,j}^{k+1} - y_{i,j}^{k}| \right\}. \tag{56}$$

The final grid is smooth and non-self-overlapping even in the presence of boundary singularities as shown in Fig. 3 which displays the final grids conforming to two different obstacles. To the best of our knowledge, this is the first time that the system of partial differential Eqs. (48) and (49) has been used to generate elliptic boundary-fitted grids. More details on the grid generation process and other grid generation alternatives can be found in [39,34,35,13,40] for similar domains.

5.2. Numerical solution of the scattering problem

The expression for Helmholtz equation in generalized curvilinear coordinates (35) is greatly simplified by substituting (46) and (47) into it. In fact, the new representation of Helmholtz equation in elliptic-polar coordinates is

$$\frac{1}{J^2}\left[\alpha(u_{in})_{\xi\xi} - 2\beta(u_{in})_{\xi\eta} + \gamma(u_{in})_{\eta\eta} + \frac{1}{2}\left(\alpha_\xi(u_{in})_\xi + \gamma_\eta(u_{in})_\eta\right)\right] + k^2 n^2 u_{in} = k^2 m u_{inc}, \tag{57}$$

where the metric factors α, β, γ, and the jacobian J were already defined in Section 4. The boundary conditions for the scattering problem in generalized curvilinear coordinates obtained in Section 4 remain unchanged in elliptic-polar coordinates.

The finite difference method is based on a second order discretization of all the derivatives present in the equations. As a result, a linear system of algebraic equations is obtained. In particular, the discrete equation corresponding to (57) has as unknowns the field values $(u_{in})_{i,j}$ in each sub-domain Ω^m. This is given by

$$\begin{aligned}
&\left(k^2 n_{i,j}^2 J_{i,j}^2 - 2(\alpha_{i,j} + \gamma_{i,j})\right)(u_{in})_{i,j} + \left(\alpha_{i,j} - \frac{1}{4}(\alpha_\xi)_{i,j}\right)(u_{in})_{i-1,j} + \left(\alpha_{i,j} + \frac{1}{4}(\alpha_\xi)_{i,j}\right)(u_{in})_{i+1,j} + \left(\gamma_{i,j} - \frac{1}{4}(\gamma_\eta)_{i,j}\right)(u_{in})_{i,j-1}\\
&+ \left(\gamma_{i,j} + \frac{1}{4}(\gamma_\eta)_{i,j}\right)(u_{in})_{i,j+1} - \frac{\beta_{i,j}}{2}\left((u_{in})_{i+1,j+1} - (u_{in})_{i+1,j-1} - (u_{in})_{i-1,j+1} + (u_{in})_{i-1,j-1}\right)\\
&= k^2 m_{i,j} J_{i,j}^2 (u_{inc})_{i,j} \quad \text{for } 1 \leqslant i \leqslant N_1^m - 1 \quad \text{and} \quad 2 \leqslant j \leqslant N_2^m.
\end{aligned} \tag{58}$$

Recall that $n_{i,j} = n(\mathbf{x}(\xi_i, \eta_j))$ with similar notation for m_{ij}. At points on each of the obstacle boundaries $\mathcal{C}^m$, the following discrete equation is derived

$$\begin{aligned}
&Z\left[\gamma_{i,1}\left(-3(u_{in})_{i,1} + 4(u_{in})_{i,2} - (u_{in})_{i,3}\right) - \beta_{i,1}\left((u_{in})_{i+1,1} - (u_{in})_{i-1,1}\right)\right] + 2(1-Z)\sqrt{\gamma_{i,1}} J_{i,1}(u_{in})_{i,1}\\
&= 2\left[\sqrt{-1}kZ\left((y_\xi)_{i,1}\cos\phi - (x_\xi)_{i,1}\sin\phi\right) - (1-Z)\sqrt{\gamma_{i,1}}\right] J_{i,1} e^{\sqrt{-1}k(x_{i,1}\cos\phi + y_{i,1}\sin\phi)}, \quad \text{for } 1 \leqslant i \leqslant N_1^m - 1.
\end{aligned} \tag{59}$$

Notice that to preserve the second order scheme and avoid the introduction of ghost points at the physical boundary, the term $(u_{in})_\eta$ of (38) has been discretized using a forward second order finite difference formula.

At each artificial boundary $\mathcal{B}^m$, the discrete Eq. (58) is evaluated at $\xi_i^m = i$ and $\eta^m = N_2^m$. As a consequence, additional unknown field values $(u_{in})_{i-1,N_2^m+1}$, $(u_{in})_{i,N_2^m+1}$ and $(u_{in})_{i+1,N_2^m+1}$ at ghost points lying outside Ω^m appear. These unknowns also

appear in the discretization of the interface condition (30), in terms of elliptic-polar grids, where (39)–(42) have been used. In fact, the discrete form of interface condition (30) at $(\xi_i^m, \eta^m) = (i, N_2^m)$ is

$$\begin{aligned}
&\frac{1}{2R^m J_{i,N_2^m}}\left[\mu_i\Big((u_{in})_{i+1,N_2^m} - (u_{in})_{i-1,N_2^m}\Big) + \lambda_i\Big((u_{in})_{i,N_2^m+1} - (u_{in})_{i,N_2^m-1}\Big)\right] \\
&\quad = \frac{k\Theta^m}{2\pi}\sum_{n=0}^{N}\epsilon_n\frac{H_n^{(1)\prime}(kR^m))}{H_n^{(1)}(kR^m)}\sum_{p=1}^{N_1^m-1}u_p^m\cos n(\theta^m(\xi_i^m) - p\Theta^m) \\
&\qquad + \sum_{l\neq m}\left\{\frac{\cos[\theta^l(\xi_i^m) - \theta^m(\xi_i^m)]k\Theta^l}{2\pi}\sum_{n=0}^{N}\epsilon_n\frac{H_n^{(1)\prime}(kr^l(\xi_i^m))}{H_n^{(1)}(kR^l))}\sum_{p=1}^{N_1^l-1}u_p^l\cos n(\theta^l(\xi_i^m) - p\Theta^l)\right. \\
&\qquad \left. + \frac{\sin[\theta^l(\xi_i^m) - \theta^m(\xi_i^m)]\Theta^l}{2\pi r^l(\xi_i^m)}\sum_{n=0}^{N}\epsilon_n\frac{nH_n^{(1)}(kr^l(\xi_i^m))}{H_n^{(1)}(kR^l)}\sum_{p=1}^{N_1^l-1}u_p^l\sin n(\theta^l(\xi_i^m) - p\Theta^l)\right\},
\end{aligned} \tag{60}$$

for $1 \leqslant i \leqslant N_1^m - 1$, and for $1 \leqslant m \leqslant M$, where $\mu_i = (x_{i,N_2^m} - b_x^m)(y_\eta)_{i,N_2^m} - (y_{i,N_2^m} - b_y^m)(x_\eta)_{i,N_2^m}$ and $\lambda_i = (y_{i,N_2^m} - b_y^m)(x_\xi)_{i,N_2^m} - (x_{i,N_2^m} - b_x^m)(y_\xi)_{i,N_2^m}$. In (60), the infinite series of eigenfunctions has been truncated up to N terms, which may destroy the uniqueness of the solution. This difficulty can be overcome by either choosing $N \geqslant \max\{kR^m\}$ (adopted in this work) or by using the modified DtN condition introduced in [16] for single scattering and in [14] for multiple scattering.

In addition, the integrals present in (42) have been approximated by the trapezoidal rule using evenly spaced partitions. The factors $\Theta^m = 2\pi/(N_1^m - 1)$ and $\Theta^l = 2\pi/(N_1^l - 1)$ are the discretization steps employed in the approximations of the integrals. Also r^l, θ^l and θ^m depend on ξ_i^m through the parametrization of the interface boundary $\mathcal{B}^m$ and through (43)–(45).

In (60), an additional family of unknowns have also appeared. They are the discrete values of the purely outgoing wave field u_p^m for $p = 1, 2, \ldots, N_1^m - 1$ and $m = 1,2,\ldots,M$ on their respective interface boundaries $\mathcal{B}^m$. Therefore, to properly complete the system of equations, we need another set of equations involving this new family of unknowns. These equations are provided by the discrete form of the interface condition (29). Substituting the expression in generalized curvilinear coordinates (39) into (29), the following discrete equation is obtained

$$(u_{in})_{i,N_2^m} = u_i^m + \sum_{l\neq m}\left\{\frac{\Theta^l}{2\pi}\sum_{n=0}^{N}\epsilon_n\frac{H_n^{(1)}(kr^l(\xi_i^m))}{H_n^{(1)}(kR^l)}\sum_{p=1}^{N_1^l-1}u_p^l\cos n(\theta^l(\xi_i^m) - p\Theta^l)\right\} \tag{61}$$

$$\text{for} 1 \leqslant i \leqslant N_1^m - 1, \text{ and for } 1 \leqslant m \leqslant M.$$

As a consequence, an algebraic linear system formed by (58)–(60) and consisting of

$$(N_1^m - 1)(N_2^m - 1) + (N_1^m - 1) + (N_1^m - 1) + (N_1^m - 1) = (N_1^m - 1)(N_2^m + 2),$$

equations for each sub-domain Ω^m have been obtained. Also, the number of unknowns on each sub-domain Ω^m includes field values at the following number of nodes:

1. The number of grid points $(N_1^m - 1) \times N_2^m$, including boundary points and without counting twice the points at the branch cut.
2. The number of ghost points: $N_1^m - 1$.
3. The number of discrete points $N_1^m - 1$ in the approximation of the purely outgoing wave field u^m.

Therefore, the total number of unknowns and total number of algebraic equations for a multiple scattering problem consisting of M obstacles is

$$\#\text{ of unknowns} = \#\text{ of equations} = \sum_{m=1}^{M}(N_1^m - 1)(N_2^m + 2). \tag{62}$$

A matrix equation for the algebraic linear system (58)–(61) is given by

$$A\mathbf{U} = \mathbf{F} \quad \text{with } A_{N_M \times N_M}, \tag{63}$$

where $N_M = \sum_{m=1}^{M}(N_1^m - 1)(N_2^m + 2)$. The construction of the unknown vector $\mathbf{U}$ depends on how the unknowns of the system are ordered. Beginning with the first obstacle ($m = 1$), the following order is implemented. To start, the discretization of the physical boundary condition (59) is used to obtain the first vector components. This means that values of the unknown field variables at the nodes $(i,1)$ for $i = 1, \ldots, N_1^m - 1$, located on the physical curve $\eta = 1$, occupy the first positions of $\mathbf{U}$. Then, values of the unknown field present in the discretization of Helmholtz equation (58) for the interior points, starting at the first node $i = 1$ of the second η-curve ($j = 2$), provides the next vector components. The next set of components comes from the unknown field values over the following η-curve (increasing j) and sweeping over the index i. This construction is repeated until the last node $i = N_1^m - 1$ of the outermost η-curve corresponding to the interface $\mathcal{B}^m$ ($j = N_2^m$) is reached. After that, unknown field values at ghost points $(i, N_2^m + 1)$, for $i = 1 \ldots N_1^m - 1$, provided by (60) are placed. The last set of unknown com-

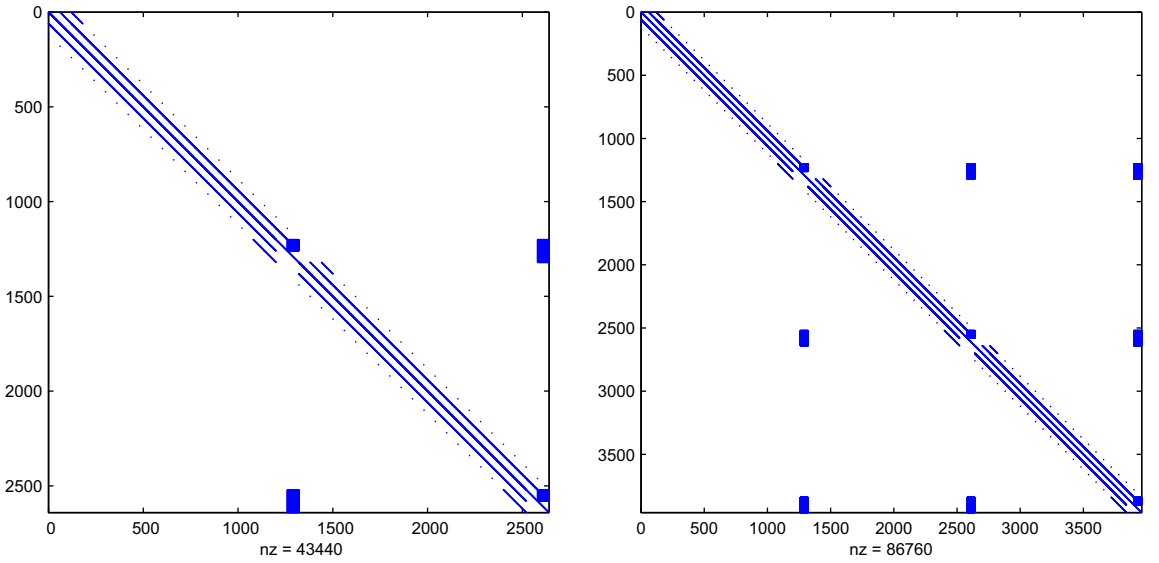

Fig. 4. Matrix pattern of A showing its non-zero entries (nz) for two obstacles (left) and three obstacles (right).

ponents corresponds to the values of the outgoing wave u^m on the boundary $\mathcal{B}^m$. They are provided by (61), for $i = 1$ until $i = N_1^m - 1$. Unknown field values for each additional obstacle ($m = 2,3,\ldots,M$) are added to $\mathbf{U}$ according to the order just described.

As a result, the unknown vector $\mathbf{U}$ has three families of entries for each obstacle. These are (i) the discrete values of the field u_{in} at each grid point, (ii) the discrete values of the field u_{in} at the ghost points lying outside the computational domain, and (iii) the discrete values of the outgoing wave fields u^m at the interface $\mathcal{B}^m$. Thus,

$$\mathbf{U} = \Big[\overbrace{(u_{in})_{1,1}\cdots(u_{in})_{N_1^1-1,N_2^1}}^{\text{at grid points}}\ \overbrace{(u_{in})_{1,N_2^1+1}\cdots(u_{in})_{N_1^1-1,N_2^1+1}}^{\text{at ghost points}}\ \overbrace{(u^1)_1\cdots(u^1)_{N_1^1-1}}^{\text{outgoing field}}\ \overbrace{\cdots}^{\text{repeat for next obstacles}}\Big]^T \tag{64}$$

The matrix A has the matrix pattern shown in Fig. 4 for two and three obstacles. A relevant feature of A is the presence of full small blocks. They are obtained from the discretization of the integrals present in the multiple-DtN boundary condition for the unknowns $u_1^m\, u_2^m, \ldots, u_{N_1^m-1}^m$. The order of the algebraic equations and unknowns may be permuted to obtain improved banded matrices, see [14]. The algebraic linear system defined by (63) is then numerically solved. We have employed the MATLAB sparse direct solver based on LU-decomposition with pivoting. This algorithm provided accurate approximations for the medium size matrices considered in this work.

6. Numerical experiments

6.1. Two cylindrical obstacles of circular cross-section

In this section, the numerical method is validated by comparing the exact solution for two circular obstacles embedded in a homogeneous medium with the numerical solution obtained from the proposed method. The analytical solution of this scattering problem and its far-field pattern can be obtained using eigenfunction expansions, as shown in [4]. The first obstacle consists of a circle of radius $a^1 = 1$ with center at $\mathbf{b}^1 = (2,-2)$. The second obstacle is a circle of radius $a^2 = 0.5$ with center at $\mathbf{b}^2 = (-2,3)$. The angle of incidence is $\phi = 0$. The interface boundary for the first sub-domain Ω_1 is a circle of radius $R^1 = 1.5$, and for the second sub-domain Ω_2, it is a circle of radius $R^2 = 1.0$. The same number of grid points was used to discretize both sub-domains. Comparisons were made for wave numbers $k = 2\pi$ and $k = 4\pi$. Boundary conditions for soft obstacles ($Z = 0$), hard obstacles ($Z = 1$), and an intermediate case ($Z = 0.5$) were considered. The approximations were obtained by truncating the series of the eigenfunction expansion (31) at $N = 50$ terms. This satisfies the requirement $N > \max\{kR^1, kR^2\}$ for these experiments. In Table 1, the maximum absolute error on the numerical far-field patterns are reported.

In order to verify the order of convergence, a sequence of numerical tests was made for increasingly finer grids conforming to the circular obstacles. More precisely, the parameter N_1 was doubled each time to obtain finer grids, while the second grid parameter N_2 was changed according to the proportion $N_1 = 6N_2$. The second order convergence of the proposed numerical method is easily verified from the results shown in Table 1. Fig. 5 displays a comparison between the exact and numerical far-field patterns for soft obstacles ($Z = 0$). The top plot was obtained for $k = 2\pi$ and $N_1 \times N_2 = 120 \times 20$. The bottom plot

Table 1
Maximum absolute error of the far-field pattern.

Grid size	$k = 2\pi$			$k = 4\pi$		
	$Z = 0.0$	$Z = 0.5$	$Z = 1.0$	$Z = 0.0$	$Z = 0.5$	$Z = 1.0$
60×10	1.12×10^{-1}	4.70×10^{-1}	3.93×10^{-1}	4.56×10^{-0}	3.63×10^{-0}	2.94×10^{-0}
120×20	2.75×10^{-2}	1.13×10^{-1}	9.61×10^{-2}	3.46×10^{-1}	9.23×10^{-1}	7.92×10^{-1}
240×40	6.91×10^{-3}	2.84×10^{-2}	2.39×10^{-2}	9.15×10^{-3}	2.36×10^{-1}	1.97×10^{-1}
480×80	1.75×10^{-3}	7.12×10^{-3}	5.96×10^{-3}	2.31×10^{-3}	5.90×10^{-2}	4.91×10^{-2}

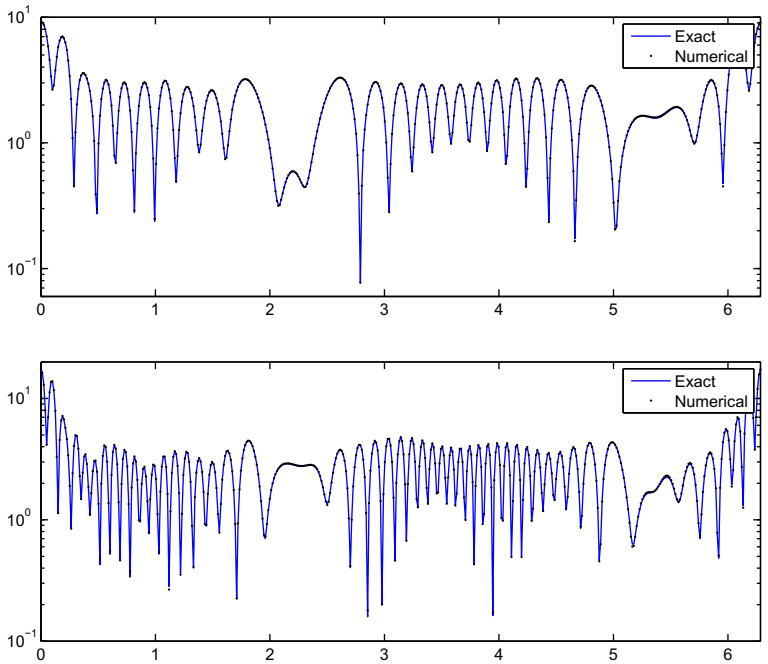

Fig. 5. Comparison between exact and numerically computed far-field patterns for two circular soft ($Z = 0$) obstacles. The wave number is $k = 2\pi$ (top), and $k = 4\pi$ (bottom).

corresponds to $k = 4\pi$ and $N_1 \times N_2 = 240 \times 40$. Even for these moderate grid sizes, excellent agreements between the approximate and the exact far-field patterns are observed. For other types of boundary conditions, similar results were obtained.

6.2. Three complexly shaped obstacles

We begin this section by showing the computational cost advantage of the multiple-DtN technique coupled with the novel elliptic-polar grids (mDtN-EPG). Multiple scattering from three obstacles bounded by complex curves is considered (see Fig. 6). The curves have the following parametric equations. The top ellipse is given by $x(t) = \frac{6}{5}\cos t$, and $y(t) = \frac{2}{5}\sin t$ with a clockwise rotation of $\pi/4$ and center at $(2\sqrt{2}, 2\sqrt{2})$. The middle three-petal rose is described by $x(t) = \frac{1}{4}(3 + \cos 3t)\cos t$ and $y(t) = \frac{1}{4}(3 + \cos 3t)\sin t$ with center at the origin. Finally, the astroid at the bottom is given by $x(t) = \frac{1}{5}(3\cos t + \cos 3t)$, and $y(t) = \frac{1}{5}(3\sin t - \sin 3t)$ with center at (0,−3). For all three shapes, $0 \leqslant t \leqslant 2\pi$. The medium is homogeneous, *i.e.*, $n \equiv 1$.

This problem was previously treated in [7] using boundary conforming grids [13] coupled with local absorbing boundary conditions [8]. The wavenumber was $k = 2\pi$. To obtain good results, a 300×300 grid consisting of 90,000 grid points was needed. The application of mDtN-EPG to this problem considerably reduces the number of grid points. In fact, for the same problem, we employ three grids of size 120×15, 120×15, and 120×20 surrounding the three scatterers. Thus, only 6000 grid points are used for the computation. This represents a 93% reduction on the domain discretization. The grids and the amplitude of the total wave field for the two different techniques are depicted in Figs. 6 and 7, respectively. Not only the number of grid points is greatly reduced, but the grid generation is independently performed on three regions containing only a single hole which significantly simplifies the generation process.

The SOR iterative method is used to solve the discrete version of the elliptic Eqs. (48) and (49). The number of unknowns is equal to the number P of grid points. Thus each iteration requires $\mathcal{O}(P)$ operations. In order to reach a level of accuracy consistent with the quadratic error of the FDM, at most $\mathcal{O}(P \ln P)$ iterations (for non-optimal relaxation parameter) are

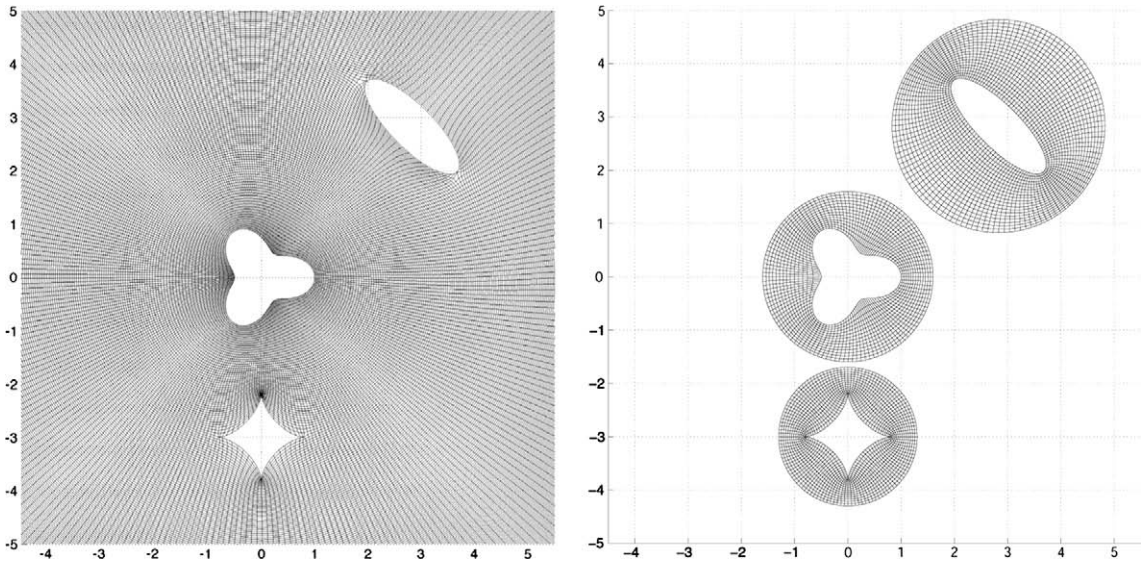

Fig. 6. Global grid (left) and mDtN-EPG local grids for three obstacles (right).

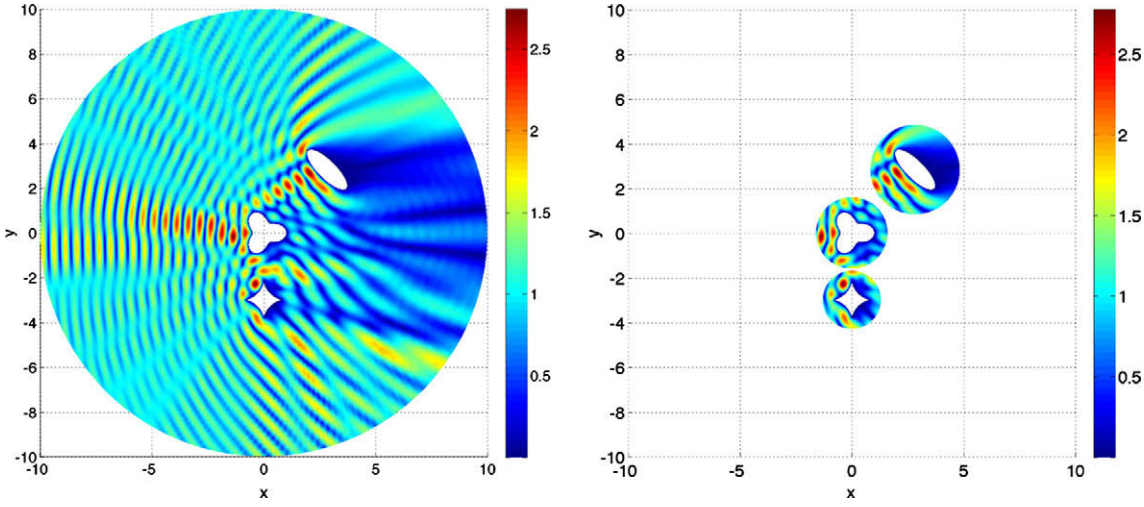

Fig. 7. Total field amplitude for multiple acoustic scattering from three obstacles using a global discretization technique coupled with local absorbing boundary condition (left) and using the mDtN-EPG technique (right).

required, see [41]. In other words, the total amount of work is $\mathcal{O}(P^2 \ln P)$. In light of this estimate, the 93% reduction in the number of grid points translates into more than 99% reduction in computational work. This is a major improvement rarely found in the literature. In addition, to generate a 120×20 grid (as in Fig. 6) only requires 0.13 s of CPU time in a modest 2.80 GHz processor using a code written in MATLAB R2008b. As a consequence the grid generation effort is minimal.

Our next experiment consists of scattering from another configuration of three complex obstacles embedded in a homogeneous medium as shown in Figs. 8 and 9. The top obstacle is bounded by the astroid given by the parametric equations $x(t) = \frac{1}{10}(4\cos t + \cos 4t)$ and $y(t) = \frac{1}{10}(4\sin t - \sin 4t)$ with a counterclockwise rotation of $\pi/5$ and center at $(-\frac{5}{4}, \frac{7}{4})$. The middle obstacle is described by $x(t) = \frac{3}{44}(10 + \cos 2t)\cos t$ and $y(t) = \frac{3}{64}(10 + 6\cos 2t)\sin t$ with a counterclockwise rotation of $\pi/2$ and center at $(-1,0)$. The bottom obstacle is given by $x(t) = \frac{3}{11}(3\cos t + \cos 3t)$ and $y(t) = \frac{3}{22}(3\sin t - \sin 3t)$ with a counterclockwise rotation of $\pi/8$ a center at $(0,-3)$. For all three shapes $0 \leqslant t \leqslant 2\pi$.

Two different boundary conditions are considered. In Fig. 8, the response for acoustically hard ($Z = 1$) obstacles is illustrated, while Fig. 9 shows the scattering from obstacles with impedance-type boundary conditions for $Z = 1/(1 + ik)$. The latter represents obstacles with absorptive boundaries. The wavenumber used for all these experiments is $k = 8\pi$. Notice that Fig. 9 exhibits a very small reflection of the incoming plane wave in the backscattered zone. In fact, its plane wave-like

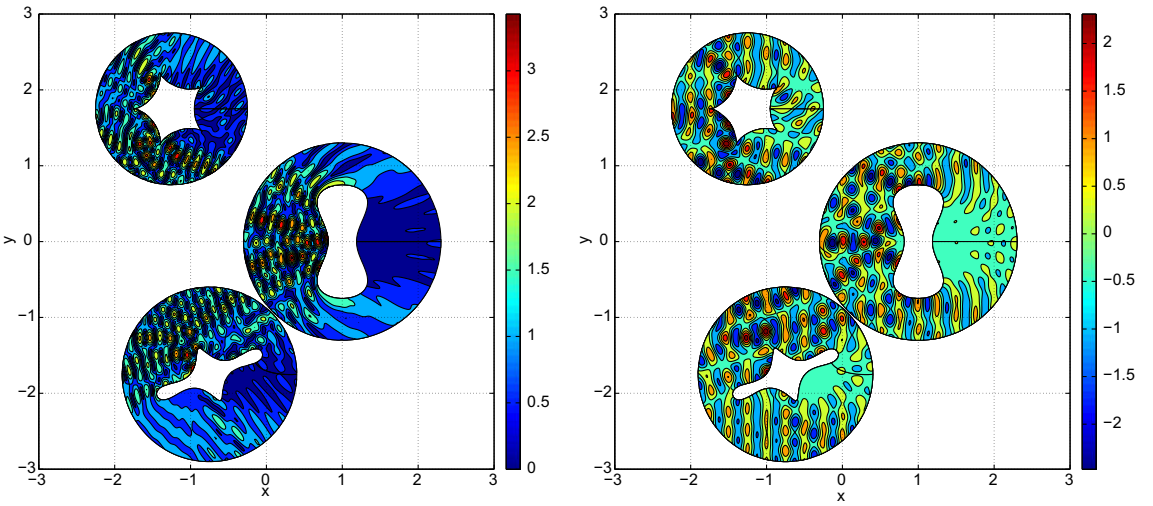

Fig. 8. Multiple acoustic scattering from three obstacles with hard-type boundary. Amplitude of the total field (left), real part of the total field (right).

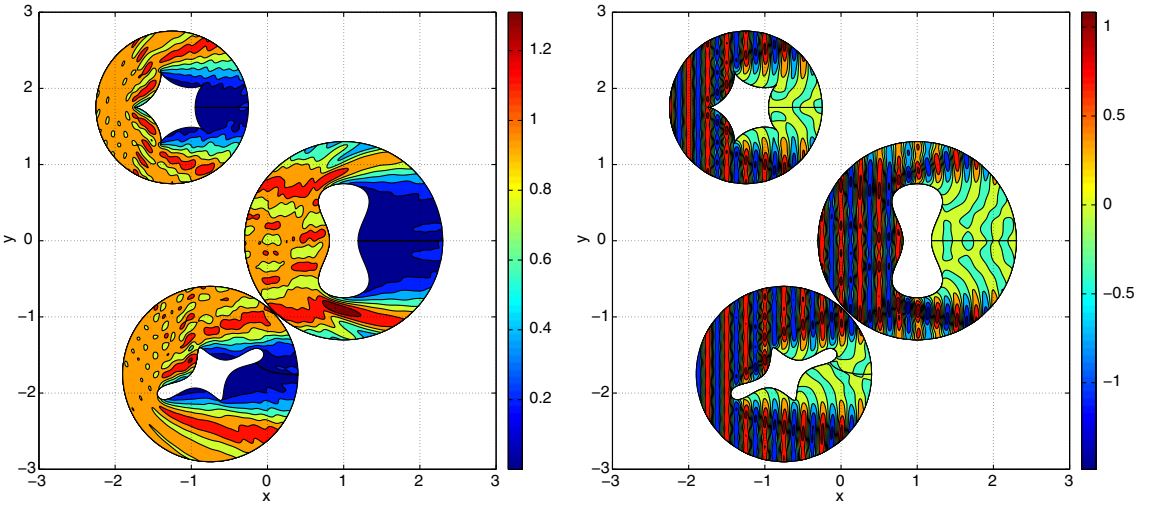

Fig. 9. Multiple acoustic scattering from three obstacles with impedance-type boundary. Amplitude of the total field (left), real part of the total field (right).

pattern are barely disturbed in this zone. This agrees with the expected physical response from absorption-type obstacles. By intentionally placing the circular interfaces of the middle and bottom obstacles very close, the continuity of the scattered field between the disjoint computational regions or sub-domains is remarkably illustrated. This fact shows how well the proposed technique handles the interaction between disjoint sub-domains.

6.3. Obstacles embedded in heterogeneous media

In this section, the numerical results for the scattering from two obstacles embedded in a locally perturbed heterogeneous medium are reported. Each obstacle is described by the parametric equations $x(t) = \frac{3}{4}(|\sin\frac{3}{2}t|^{10} + |\cos\frac{3}{2}t|^{10})^{-1/10}\cos t$, and $y(t) = \frac{3}{4}(|\sin\frac{3}{2}t|^{10} + |\cos\frac{3}{2}t|^{10})^{-1/10}\sin t$, with $0 \leqslant t \leqslant 2\pi$. The obstacles are centered at the points $(-4,0)$ and $(4,0)$, respectively. The angle of incidence is $\phi = \pi/2$ and the wavenumber is $k = \pi$. The scatterers possess acoustically soft boundaries. For an obstacle centered at the origin, the index of refraction n is defined as follows:

$$n(x,y) = n(\rho) := \begin{cases} 4, & \text{if } \rho \leqslant 1.25, \\ 0.5(3\cos(2\pi(\rho - 1.25)) + 5), & \text{if } 1.25 \leqslant \rho \leqslant 1.75, \\ 1, & \text{if } 1.75 \leqslant \rho, \end{cases}$$

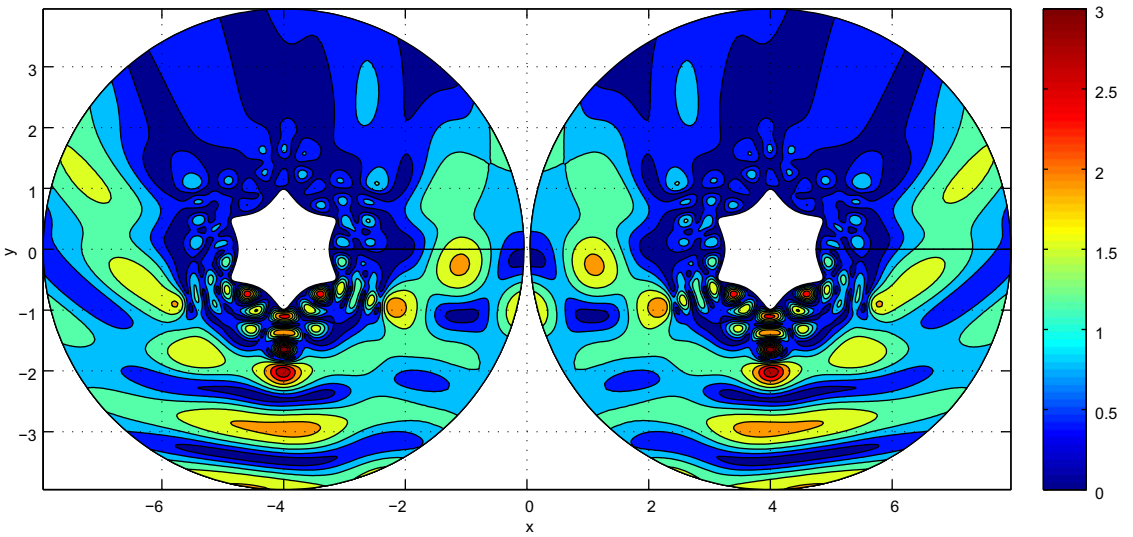

Fig. 10. Multiple scattering from two obstacles embedded in a heterogeneous medium. Amplitude of the total field when angle of incidence $\phi = \pi/2$, wavenumber $k = \pi$, for acoustically soft obstacles.

where $\rho(x,y) := r(|\sin\frac{3}{2}\theta|^{10} + |\cos\frac{3}{2}\theta|^{10})^{1/10}$, and (r,θ) are the polar coordinates of a point $(x,y) \in \Omega$. This definition of n needs to be translated to the center of each obstacle. Hence, the index of refraction changes smoothly from a maximum of *4* at the boundary of the obstacles to a minimum of *1* far from them. In other words, the effective wavenumber reaches a maximum of four times the wavenumber of the incident field close to the obstacles. In Fig. 10, the expected physical behavior that the wavelength of the total field is much smaller in the heterogeneous region than outside of it is illustrated. This particular experiment shows the applicability of the FDM coupled with the DtN condition to handle scattering from localized heterogeneous media.

7. Conclusions

Multiple scattering problems from complexly shaped obstacles have been numerically solved. We have considered not only scatterers inside otherwise homogeneous media, but also the more challenging case of obstacles embedded in heterogeneous media with variable index of refraction in their vicinity.

Our approach consists of replacing the original exterior problem by an equivalent interface problem whose interface $\mathcal{B}$ is formed by closed smooth boundaries $\mathcal{B}^m$ that serve as separate artificial boundaries for each obstacle. Then, numerical solutions are obtained inside the relatively small annular regions containing each obstacle. This has two major advantages. One of them is that the number of grid points is greatly reduced compared with those obtained from enclosing all the scatterers by a single boundary. The other is that the grid generation is independently performed on the regions containing only a single obstacle which significantly simplifies the generation process. This is particularly true for the structured grids supporting the finite difference methods employed in this work. As a result, the computational cost is greatly reduced.

We also provide a rigorous proof for the equivalence between the interface BVP and the original multiple scattering problem that accounts for the presence of localized media heterogeneities. The proof, based on Green's integral representation formula, does not require the use of separable coordinate systems or the knowledge of a particular set of eigenfunctions.

To illustrate the practical value of the technique, we applied it to challenging scatterer configurations as shown in Figs. 7–10. Qualitative results coincide with the physical expectation for the scattering from these configurations. Moreover, the circular interfaces of the neighbor obstacles were intentionally placed very close and the continuity of the scattered field between disjoint computational regions or sub-domains was remarkably observed. We also obtained accurate approximations of the wave field and far-field pattern for the benchmark problem of scattering from two circular cylinders (see Fig. 5). In fact, a comparison with the exact solution easily revealed a second order convergence for our second order method.

Finite difference methods are attractive for the simulation of wave phenomena due to their simplicity and efficiency on cartesian grids for geometrically simple domains. However, their application on complex geometries may be negatively affected by the grid choice. For instance, using cartesian staircase-type meshes, the convergence rate of a classical second order scheme may be reduced to first order, as described in [42,43]. More recent comparisons performed by Medvinsky et al. [12] found that the errors using FEM were larger than using finite differences for single scattering from elliptical obstacles. They attributed it to the inaccuracies in approximating the elliptical boundary with a polar grid when using the FEM. These results motivated our choice of smooth and boundary-conforming grids, such as the novel elliptic-polar grids introduced in Section 5.1, for our numerical scheme.

Although the computations of the multiple-DtN technique are performed in relatively small sub-domains, the linear system that results from the discretization of the continuous problem is not completely sparse. In fact, all the field values at the interface are also part of the unknowns. This may be a disadvantage when compared with the integral equation methods, such as Nyström or boundary elements, whose matrices are dense but their only unknowns are at the obstacle boundaries. However, when the properties of the medium change, the use of integral equation methods may result in comparable or larger linear systems than those obtained by employing the proposed method.

We are currently working on the implementation of the theoretical results found in this work to configurations of truly complex three-dimensional obstacles. One of the major challenges in doing this will be the extension of the grid generation technique to three-dimensional scatterer configurations. However, the fact that grids are independently generated in subdomains containing a single obstacle will greatly simplify the process. In order to improve the rate of convergence and the computational efficiency, we plan to use higher order compact schemes [44] instead of our current second order method.

Acknowledgments

The authors thank the anonymous referees for their most constructive suggestions which certainly improved the quality of the manuscript. The first author's work was supported by the Office of Research and Creative Activities (ORCA) of Brigham Young University.

References

[1] Y. Huang, Y. Lu, Scattering from periodic arrays of cylinders by Dirichlet-to-Neumann maps, J. Lightwave Technol. 24 (2006) 3448–3453.
[2] X. Antoine, C. Chniti, K. Ramdani, On the numerical approximation of high-frequency acoustic multiple scattering problems by circular cylinders, J. Comput. Phys. 227 (2008) 1754–1771.
[3] P. Gabrielli, M. Mercier-Finidori, Acoustic scattering by two spheres: multiple scattering and symmetry considerations, J. Sound Vibr. 241 (2001) 423–439.
[4] P. Martin, Multiple Scattering, Cambridge University Press, 2006.
[5] S. Sherer, M. Visbal, High-order overset-grid simulations of acoustic scattering from multiple cylinders, in: Proceedings of the Fourth Computational Aeroacoustics (CAA) Workshop on Benchmark Problems, NASA/CP-2004-212954, 2004, pp. 255–266.
[6] S.E. Sherer, J.N. Scott, High-order compact finite-difference methods on general overset grids, J. Comput. Phys. 210 (2005) 459–496.
[7] V. Villamizar, S. Acosta, Generation of smooth grids with line control for scattering from multiple obstacles, Math. Comput. Simulat. 79 (2009) 2506–2520.
[8] A. Bayliss, E. Turkel, Boundary conditions for the numerical solution of elliptic equations in exterior regions, SIAM J. Appl. Math. 42 (1982) 430–451.
[9] D. Givoli, Non-reflecting boundary conditions, J. Comput. Phys. 94 (1991) 1–29.
[10] D. Givoli, High-order non-reflecting boundary conditions, Wave Motion 39 (2004) 319–326.
[11] S. Tsynkov, Numerical solution of problems on unbounded domains. A review, Appl. Numer. Math. 27 (1998) 465–532.
[12] M. Medvinsky, E. Turkel, U. Hetmaniuk, Local absorbing boundary conditions for elliptical shaped boundaries, J. Comput. Phys. 227 (2008) 8254–8267.
[13] V. Villamizar, O. Rojas, J. Mabey, Generation of curvilinear coordinates on multiply connected regions with boundary singularities, J. Comput. Phys. 223 (2007) 571–588.
[14] M. Grote, C. Kirsch, Dirichlet-to-Neumann boundary conditions for multiple scattering problems, J. Comput. Phys. 201 (2004) 630–650.
[15] J. Keller, D. Givoli, Exact non-reflecting boundary conditions, J. Comput. Phys. 82 (1989) 172–192.
[16] M. Grote, J. Keller, On nonreflecting boundary conditions, J. Comput. Phys. 122 (1995) 231–243.
[17] S. Cummer, B. Popa, D. Schurig, D. Smith, J. Penry, Full-wave simulation of electromagnetic cloaking structures, Phys. Rev. E 74 (2006) 036621.
[18] F. Guevara-Vasquez, G. Milton, D. Onofrei, Active exterior cloaking for the 2D Laplace and Helmholtz equations, Phys. Rev. Lett. 103 (2009) 073901.
[19] R. Maccamy, S. Marin, A finite element method for exterior interface problems, Int. J. Math. Sci. 3 (1980) 311–350.
[20] F. Ihlenburg, Finite Element Analysis of Acoustic Scattering, Springer, 1998.
[21] C. Johnson, J. Nedelec, On the coupling of boundary integral and finite element methods, Math. Comput. 35 (1980) 1063–1079.
[22] G. Hsiao, Some recent development on the coupling of finite element and boundary element methods, Rend. Sem. Mat. Univ. Pol. Torino (1991) 96–111.
[23] G. Hsiao, E. Schnack, W. Wendland, A hybrid coupled finite-boundary element method in elasticity, Comput. Methods Appl. Mech. Eng. 173 (1999) 287–316.
[24] A. Kirsch, P. Monk, A finite element/spectral method for approximating the time-harmonic maxwell system in $\mathbb{R}^3$, SIAM J. Appl. Math. 55 (1995) 1324–1344.
[25] B. Despres, Domain decomposition method and the Helmholtz problem, in: G. Cohen, P. Joly, L. Halpern (Eds.), First International Conference on Mathematical and Numerical Aspects of Wave Propagation, SIAM, Strasbourg, Fr., 1991, pp. 44–52.
[26] P. Monk, Finite Element Methods for Maxwell's Equations, Oxford University Press, 2003.
[27] D. Colton, R. Kress, Inverse Acoustic and Electromagnetic Scattering Theory, second ed., Springer, 1998.
[28] G. Roach, Green's Functions, second ed., Cambridge University Press, 1982.
[29] P. Grisvard, Elliptic Problems in Nonsmooth Domains, Pitman Publishing Inc., 1985.
[30] Z. Yosibash, M. Arad, A. Yakhot, G. Ben-Dor, An accurate semi-analytical finite difference scheme for two-dimensional elliptic problems with singularities, Numer. Methods Partial Differ. Eqn. 14 (1998) 281–296.
[31] X. Cheng, A. Shaikh, Iterative methods for the Poisson equation in L-shape domain based on domain decomposition, Appl. Math. Comput. 180 (2006) 393–400.
[32] D. Givoli, L. Rivkin, J. Keller, A finite element method for domains with corners, Int. J. Numer. Methods Eng. 35 (1992) 1329–1345.
[33] X. Wu, H. Han, A finite-element method for Laplace- and Helmholtz-type boundary value problems with singularities, SIAM J. Numer. Anal. 34 (1997) 1037–1050.
[34] P. Knupp, S. Steinberg, Fundamentals of Grid Generation, CRC Press, 1993.
[35] J.F. Thompson, B.K. Soni, N.G. Weatherill, Handbook of Grid Generation, CRC Press, 1999.
[36] S.H. Lee, B.K. Soni, The enhancement of an elliptic grid using appropriate control functions, Appl. Math. Comput. 159 (2004) 809–821.
[37] J.F. Thompson, A general three-dimensonal elliptic grid generation system on a composite block structure, Comput. Methods Appl. Mech. Eng. 64 (1987) 377–411.
[38] J. Strikwerda, Finite Difference Schemes and Partial Differential Equations, second ed., SIAM, 2004.
[39] S. Acosta, V. Villamizar, Finite difference on grids with nearly uniform cell area and line spacing for the wave equation on complex domains, J. Comput. Appl. Math. (2009), doi:10.1016/j.cam2009.08.048.

[40] V. Villamizar, S. Acosta, Elliptic grids with nearly uniform cell area and line spacing, Electron. Trans. Numer. Anal. 34 (2009) 59–75.
[41] R. LeVeque, Finite Difference Methods for Ordinary and Partial Differential Equations, SIAM, 2007.
[42] A. Cangellaris, D. Wright, Analysis of the numerical error caused by the stair-stepped approximation of a conducting boundary in FDTD simulations of electromagnetic phenomena, IEEE Trans. Antennas Propog. 39 (1991) 1518–1525.
[43] R. Holland, Pitfalls of staircase meshing, IEEE Trans. Electromag. Comp. 35 (1993) 434–439.
[44] S.K. Lele, Compact finite difference schemes with spectral-like resolution, J. Comput. Phys. 103 (1992) 16–42.